Supplementary Information

Magnesium chloride salt-assisted synthesis of porous N-doped carbons from molten polycyclic aromatic hydrocarbons for high-performance supercapacitors

Keren Barchichat,[a] Alagar Raja Kottaichamy,*[a,b,c] Michael Volokh,[a] Rotem Geva,[a] Alexander Upcher,[d] Jonathan Tzadikov,*[a] Jesús Barrio,[e] and Menny Shalom*[a,d]

a. Department of Chemistry, Ben-Gurion University of the Negev, Beer-Sheva 8410501, Israel.
b. Academy of Scientific and Innovative Research (AcSIR), Ghaziabad 201002, India.
c. Electrochemical Power Sources Division, CSIR-CECRI, Karaikudi 360003, Tamil Nadu, India.
d. Ilse Katz Institute for Nanoscale Science and Technology, Ben-Gurion University of the Negev, Beer-Sheva 8410501, Israel.
e. Department of Chemical Engineering, Imperial College London, London SW7 2AZ, UK.

*Correspondence: alagarraja.cecri@csir.res.in; tzadikov@bgu.ac.il; mennysh@bgu.ac.il

Supplementary Information Table of Contents

1. Materials and Reagents

All chemicals were purchased from commercial vendors and used as received without further purification. 1,10-Phenanthroline (Ph, 99%) and pyrene (Py, 98%) from Thermo Scientific; magnesium chloride hexahydrate ($MgCl_2 \cdot (H_2O)_6$, 99.999%) and Nafion solution (5 wt.% in 2-propanol, *n*-propanol, and water) from Sigma-Aldrich; concentrated hydrochloric acid (HCl, 32% wt., AR grade) and concentrated nitric acid (HNO_3, 70% wt., AR grade) from Bio-lab (Israel); isopropyl alcohol (IPA, HPLC electrochemical grade 2-propanol) from Fisher Chemicals, employed for ink preparation; YP-50F carbon from Kuraray Chemicals (India). All experiments utilized deionized (DI) water, obtained using a Millipore MilliQ Direct 3 purification system (18.2 MΩ cm resistivity at room temperature).

2. Nitrogen-Doped Carbons (NdCs) Synthesis

Pyrene (Py), 1,10-phenanthroline (Ph), and magnesium chloride hexahydrate (abbreviated as Mg for simplicity) were used as the starting materials. The various mixtures of precursors are denoted as $Ph_1Py_xMg_t$, where *x* and *t* represent the relative analytical weights of Py and Mg, respectively, with Ph set as 1 constantly; see Table S1. When the abbreviation Ph_1Py_x is used, the template ratio remains constant across all samples, corresponding to a tenfold excess of Mg with respect to Ph (*i.e.*, Ph_1Py_x is a shorthand for $Ph_1Py_xMg_{10}$).

Initially, each precursor was weighed with analytical precision into a ceramic crucible, and the components were mixed. The crucible was then introduced into a muffle furnace, under constant nitrogen (N_2; 99.999%) flow (inert atmosphere) and subjected to the following thermal treatment: the temperature was increased to 90 °C and held for 1 h; it was then ramped at 2.5 °C min^{-1} to 170 °C and maintained for 1 h. Thereafter, the temperature was further raised at 2.5 °C min^{-1} to 800 °C and sustained for 4 h at this target temperature, after which natural cooling ensued down to room temperature (*rt*).

The solid product was subsequently ground and underwent a series of washing steps: it was washed twice with DI water, then with 2 M hydrochloric acid, and finally washed twice more with DI. All washing steps, aside from the final DI wash (24 h), were conducted on a stirring plate (300 rpm, *rt*) over 72 h, followed by centrifugation (6000 rpm, *rt*, 10 min). The last wash was carried out *via* Buchner vacuum filtration using a nylon filtration paper (0.22 μm). Finally, the washed material was dried at 60 °C for 24 h on a glass petri dish.

Table S1. Mass and mol ratios of pyrene-to-1,10-phenanthroline precursors in Ph_1Py_x.

Sample	Mass ratio (m_{Py} m_{Ph}^{-1})	Mol ratio (n_{Py} n_{Ph}^{-1})	Mol ratio (n_{Py} n_{Mg}^{-1})
Ph_1Py_0	0	0	17.8
$Ph_1Py_{0.5}$	0.50	0.45	17.8
Ph_1Py_1	1.0	0.90	17.8
$Ph_1Py_{1.5}$	1.5	1.3	17.8

3. Characterization Methods

X-ray diffraction (XRD) analysis of the products was performed on a PANalytical Empyrean diffractometer equipped with a position-sensitive PIXcel3D detector. The data was acquired over a 17-minute scan, with 2θ values ranging from 10° to 90°, using Cu Kα radiation (λ = 1.54874 Å, 40 kV, 30 mA).

Raman spectra of the products, as well as of the electrode surfaces before and after acidic treatment and supercapacitor (SC) application (post-operation), were collected using a confocal Horiba LabRam HR evolution micro-Raman system, equipped with Syncerity Open Electrode CCD detector (deep-cooled to –60 °C, 1024 × 256 pixels). The light source was a 532 nm laser at ~0.3–0.9 mW on the sample. The laser was focused on the sample surface with LMPlanFL N ×50/ 0.5 objective (Olympus). The measurements were taken using 100 μm confocal hole and 1800 grooves mm^{-1} grating, followed by spectral resolution of about 0.5 cm^{-1} $pixel^{-1}$, with a spot size of ~1.3 μm. Auto-calibration procedure was performed using a Labspec software (Horiba, version 6.5.2) over a single-crystal silicon wafer (111). The spectra were taken at the range of 800–3500 cm^{-1} for 20 s exposure time, corrected for baseline by the Labspec software.

X-ray photoelectron spectroscopy (XPS) measurements were conducted on an ESCALAB 250 ultrahigh vacuum spectrometer (1×10^{-9} bar) using an Al Kα X-ray source and a monochromator that produced a 500 μm beam. A survey spectrum was initially recorded at a pass energy (PE) of 150 eV, followed by high-resolution spectra at PE = 20 eV; all spectra were calibrated relative to the carbon C 1s peak at 284.8 eV to correct for charging effects. Background subtraction for XPS analysis was performed using Avantage software (Thermo Scientific) and the data were subsequently fitted with fityk software.

Scanning electron microscopy (SEM) was carried out using a FEI Verios 460L high-resolution SEM featuring a field emission gun (FEG) and a through-lens detector (TLD) for secondary electrons detection, operated at 5.0 kV with a probe current of 25 pA. Energy

dispersive X-ray spectrometry (EDS) analysis was performed on the same instrument using an Oxford Xmax 80 mm^2 127 eV Si drift detector while the SEM was operated at 20.0 kV to analyze the elemental composition.

Scanning/transmission electron microscopy (S/TEM) analysis was obtained using Spectra 200 (Thermo Fisher Scientific) equipped with a probe Cs-corrector (S-CORR) and cold-FEG electron source at an accelerating voltage of 200 kV. In transmission electron microscopy (TEM) mode, the images were recorded with Ceta-M CMOS camera. In scanning transmission electron microscopy (STEM) mode, the images were recorded with high angle annular dark field (HAADF) detector, and the energy dispersive X-ray spectroscopy (EDS) spectra were collected with Super-X (Thermo Fisher Scientific) silicon drift detector (SDD). The images and the EDS spectra were processed with Thermo Fisher Scientific Velox software (version 3.19).

Two types of analytical elemental analysis methods were used: (a) organic elemental analysis (EA) using a Thermo Scientific CHNS Analyzer (Flash2000), and (b) inductively coupled plasma–optical emission spectroscopy (ICP–OES) using an Arcos FHM22 spectrometer in an axial configuration. For ICP–OES sample preparation, 5.00 mL of concentrated 70% wt. HNO_3 was added to 10 mg of each sample and heated overnight in a autoclave oven for 12 hours at 130 °C; after cooling to *rt*, 1.00 mL of the solution was diluted (×10) to 10.00 mL with DI water for analysis.

Thermogravimetric analysis (TGA) of the products was performed using a Setaram LABSYS evo TGA instrument. Approximately 10–20 mg of the precursors' mixture was placed in alumina crucibles and heated under the same conditions as those used during the reported synthesis (constant N_2 flow of 10 sccm).

Nitrogen physisorption isotherms were measured at 77 K using a Quantachrome Autosorb-iQ2 sorptometer, with specific surface areas determined *via* the Brunauer–Emmett–Teller (BET) method; total pore volume calculated at a relative pressure ($P\ P_0^{-1}$) of 0.99; the pore size distribution was obtained using quenched solid density functional theory (QSDFT) analysis provided by the instrument's software (ASiQwin version 5.2).

Optical contact angle (OCA) measurements (repeated three times) were collected using an OCA system from DataPhysics Instrument. Fig.S9 presents snapshots from video of a single measurement out of the three (Table S10).

Zeta potential (ζ-P) analysis (ZPA) of $Ph_1Py_{0.5}$ and YP-50F was performed using a Malvern Zetasizer (Nano ZS) instrument from Anton Paar using a Malvern folded capillary cell. The analysis was carried out using Zetasizer 7.02 software with the built-in parameters for water,

applying the Smoluchowski approximation for calculation of the ζ-P from the electrophoretic mobility measurements; for this analysis, 2 mg of each sample was dissolved in 1 mL IPA, sonicated for 2 hours, and 50 µL of the resulting solution was added to 1 mL of 5 mM H_2SO_4 and sonicated for 30 min. The experiments were conducted at controlled T = 25 °C with DI as the solvent; the operation voltage was set to 40 V.

4. Electrochemical Methods

All the electrochemical experiments were carried out using BioLogic VSP3e potentiostat. The measurements were conducted in a 10 mL three-electrode cell configuration, utilizing a glassy carbon (GC, 3 mm) working electrode (WE), a graphite wire counter electrode (CE), and an Ag/AgCl (saturated KCl) reference electrode (RE) immersed in 0.5 M H_2SO_4 electrolyte. To prepare the WE for measurement, an ink was prepared: 400 µL IPA and 15 µL Nafion (5 wt. %) were added to 5 mg of the active material in a glass vile and sonicated for 3 h. 5 µL of this freshly sonicated ink was drop-case on the GC electrode and air-dried. Prior to each measurement, the GC electrode was polished with 0.05 µm alumina powder and the electrolyte solution was purged with argon for 1 h. The bare GC electrode underwent electrochemical cleaning by cycling the potential between –0.2 and 0.8 V *versus* (*vs*) reversible hydrogen electrode (RHE) in 0.5 M H_2SO_4 three times before ink deposition.

All measured potentials were converted to the reversible hydrogen electrode (RHE) scale for reporting using the Nernst equation at *rt* as shown in Equation S1:

$$E_{RHE} = E_{Ag/AgCl} + 0.197\ V + 0.059 \times pH \qquad \text{(Eq. S1)}$$

Where E_{RHE} stands for the potential referred to reversible hydrogen electrode, $E_{Ag/AgCl}$ is the potential of the reference electrode, is the standard potential of the reference electrode (Ag/AgCl with saturated potassium chloride solution), and pH is the Ph measured of the electrolyte solution.

5. SI Figures and Tables—Synthesis and Material Characterization

a. Synthesis of nitrogen-doped carbons (NdCs)

Detailed synthetic conditions and explanation

Initially, the mixture was heated to 90 °C for 1 h to remove residual moisture. Subsequently, the temperature was increased from 90 °C to 170 °C (ramp rate 2.5 °C min^{-1}) and maintained for 1 h, exceeding the melting points of Ph (117 °C), Mg (117 °C) and Py (148 °C), to ensure complete phase transition of Ph, Py, and Mg. According to Xu *et al.*, who examined the influence of heating rates on Mg complex decomposition,[1] dehydration of Mg to solid magnesium chloride tetrahydrate occurs prior to reaching 117 °C, where Mg melting takes place. Between 117 °C and 170 °C, further dehydration of $MgCl_2 \cdot 4H_2O$ yields magnesium chloride dihydrate ($MgCl_2 \cdot 2H_2O$), which undergoes hydrolysis to form magnesium chloride ($MgCl_2$) and magnesium hydroxychloride (Mg(OH)Cl) within the temperature range of 170–240 °C. Finally, heating from 170 °C to 800 °C at 2.5 °C min^{-1} for 4 h induces carbonization of Ph and Py, accompanied by morphology-controlled polymerization. The polymerization process is guided by the *in-situ* formation of a MgO hard template, originating from the decomposition of Mg(OH)Cl and $MgCl_2$.[1–3] Since MgO is thermally stable under the carbonization temperature (800 °C), it acts as a rigid scaffold during carbonization, where carbon forms around the MgO nanoparticles.[4]

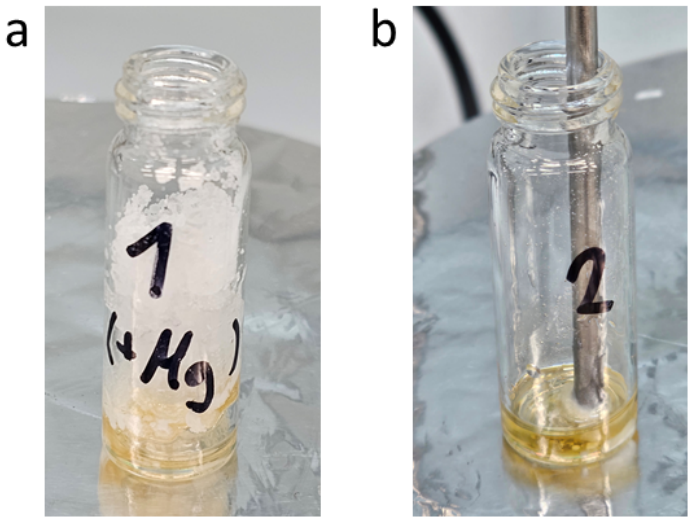

Fig. S1 Illustration of the melting process of precursors mixtures of $Ph_1Py_{0.5}Mg_{10}$ (a, with Mg) and $Ph_1Py_{0.5}$ (b, without Mg) under identical conditions. The samples are shown *ca.* 170 °C (the melting point of Py), where both samples exhibit a molten state.

Upon heating the hotplate to 170 °C, a molten state is evident in both samples. The 'internal' temperatures (measured using thermocouple) indicated values of 111 and 122 °C for $Ph_1Py_{0.5}$ and $Ph_1Py_{0.5}Mg_{10}$, respectively.

Yield calculation

The yield (%) of each product was calculated using Equation S2, assuming a theoretical yield of 100%. The results are summarized in Table S1.

$$\text{Yield (\%)} = \frac{m_f}{m_i} \times 100\% \qquad \text{(Eq. S2)}$$

Where m_i is the total initial combined analytical mass of Ph and Py and m_f is the mass of the product (after washing and removal of Mg).

Table S2. Yields of the products according to Equation S2.

Sample	Yield
Ph_1Py_0	53%
$Ph_1Py_{0.5}$	22%
Ph_1Py_1	25%
$Ph_1Py_{1.5}$	28%

Large scale synthesis of $Ph_1Py_{0.5}$

Fig. S2 Large-scale synthesis demonstration of $Ph_1Py_{0.5}$. (a–b) $Ph_1Py_{0.5}$ after synthesis using a muffle furnace, (c) analytical weight of $Ph_1Py_{0.5}$ (m = 51.9075 g).

b. X-ray diffraction (XRD)

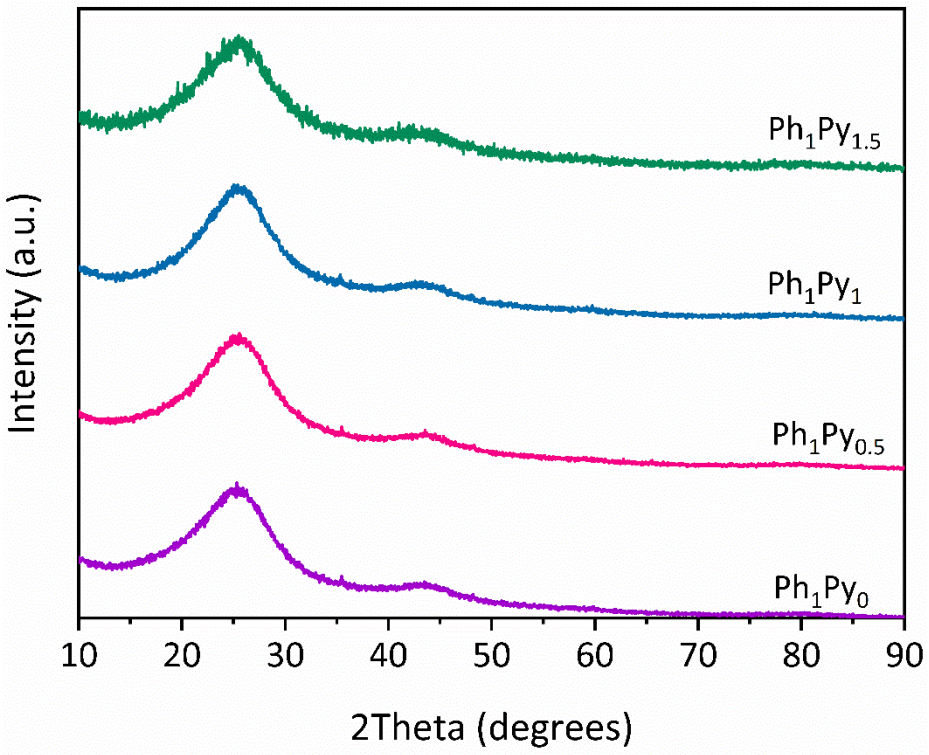

Fig. S3 XRD patterns of Ph_1Py_x. The patterns are vertically offset for clarity.

The XRD patterns exhibit characteristic graphitic diffraction signals, accompanied by a lower degree of crystallinity. The diffractions *ca.* 27° are attributed to the (002) planes, representing the spacing between two adjacent crystal planes. Its broadness suggests lower crystallinity, compared to graphite. We ascribe it to nitrogen doping, which creates defects in the structures. The diffractions *ca.* 43°, correspond to the (101) plane, related to the in-plane orientation of the structure.[5,6]

Bragg law calculation

Bragg's law, shown in Equation S3,[6] was applied to evaluate the interplanar spacing, with the corresponding *d*-spacing values calculated by assuming first order diffractions (n = 1) and rearranging Equation S3 into Equation S4.

$$2d \sin\theta = n\lambda \qquad \text{(Eq. S3)}$$

$$d = \frac{\lambda}{2 \sin\theta} \qquad \text{(Eq. S4)}$$

Where d is the separation of scattering planes, λ is the wavelength of the incident X-ray beam (see experimental details), and θ is the angle between the incident and scattered beams.

Table S3. Calculated Ph_1Py_x *d*-spacing values from Bragg's law analysis.

Sample	Mass ratio (m_{Mg} m_{Ph}^{-1})	*d*-spacing (nm)
Ph_1Py_0	10	0.362
$Ph_1Py_{0.5}$		0.359
Ph_1Py_1		0.366
$Ph_1Py_{1.5}$		0.360
$Ph_1Py_{0.5}Mg_0$	0	0.362

A smaller *d*-spacing indicates reduced interlayer distance, reflecting stronger π–π stacking interactions within the structure.[5,7]

c. Raman spectroscopy

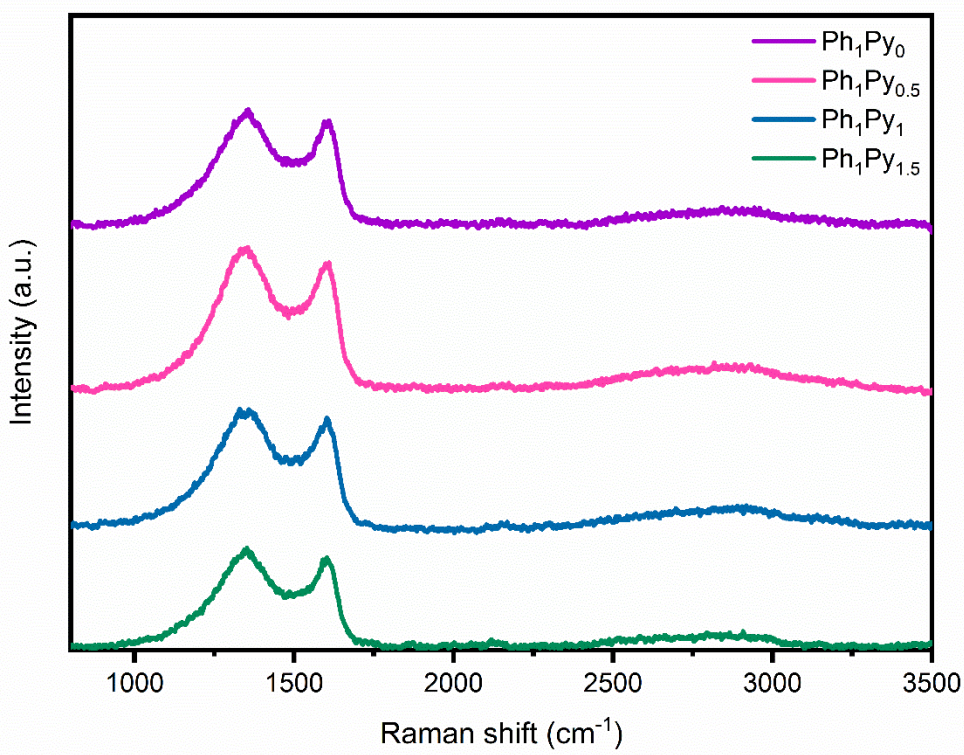

Fig. S4 Raman spectra of the different Ph_1Py_x products. The spectra are vertically offset for clarity.

Table S4. I_D/I_G ratios (Raman analysis of the fitted spectra) of the products and of the carbon electrode before and after SC operation.

Sample	Mass ratio (m_{Mg} m_{Ph}^{-1})	Raman shift (cm^{-1})		I_D/I_G
		D band	G band	
$Ph_1Py_{0.5}Mg_0$	0	1351.0	1603.0	1.075
Ph_1Py_0	10	1340.5	1614.5	1.076
$Ph_1Py_{0.5}$		1344.7	1617.2	1.186
Ph_1Py_1		1346.7	1619.5	1.162
$Ph_1Py_{1.5}$		1343.2	1614.7	1.216

d. X-ray photoelectron spectroscopy (XPS)

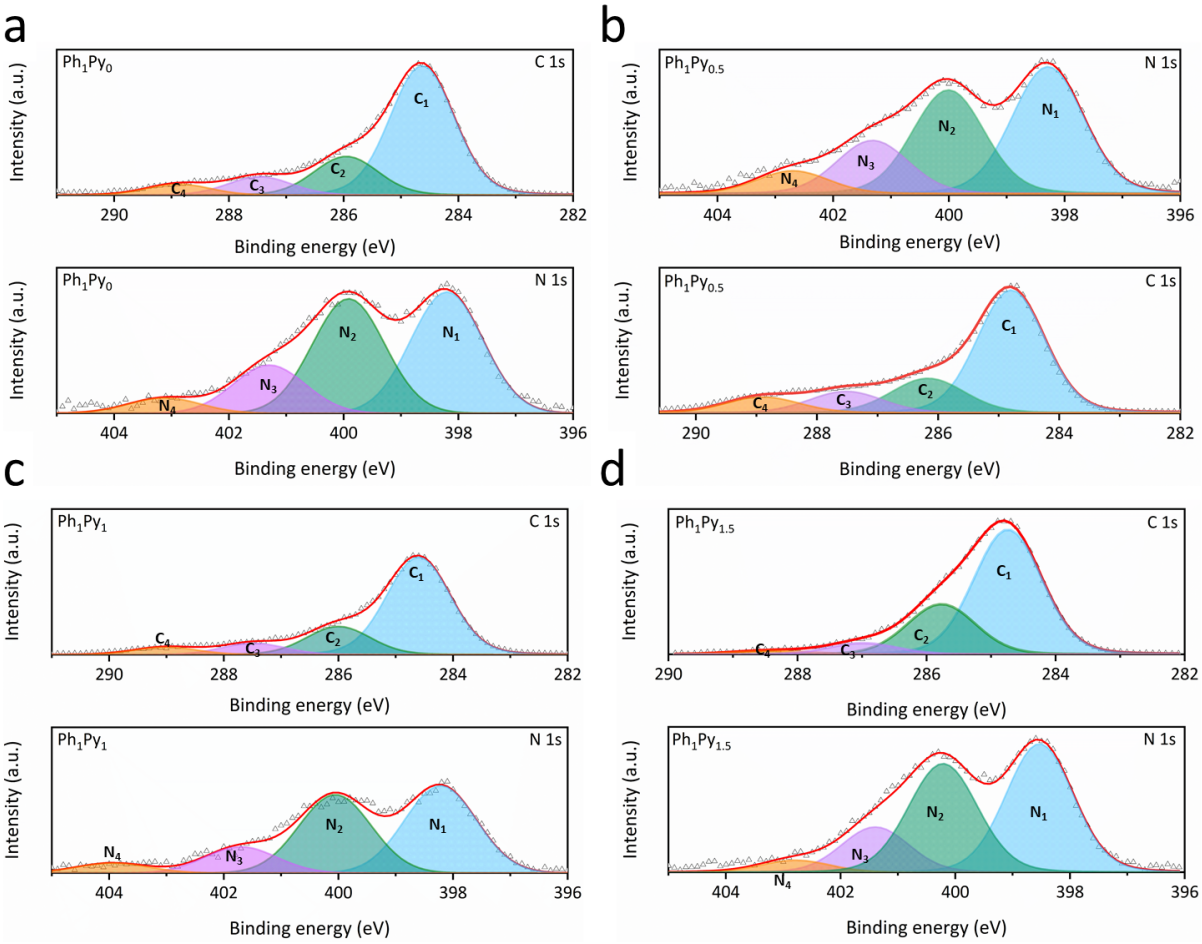

Fig. S5 C 1s and N 1s XPS spectra of (a) Ph_1Py_0, (b) $Ph_1Py_{0.5}$, (c) Ph_1Py_1, and (d) $Ph_1Py_{1.5}$. The experimental data points (triangles) are fit (red curve) and deconvoluted into four peaks for each spectrum, labelled C_1–C_4 and N_1–N_4 for C 1s and N 1s, respectively.

Table S5. Relative atomic percentage of carbon and nitrogen species.

Sample	**C 1s relative abundance (at. %)**				**N 1s relative abundance (at. %)**			
Species	C_1	C_2	C_3	C_4	N_1	N_2	N_3	N_4
	sp^2	C–N/C–O	R-C=N/R-C=O	O–C=O	Pyridinic	Pyrrolic	Graphitic	N–O_x
Ph_1Py_0	67	19	9	5	40	38	16	5
$Ph_1Py_{0.5}$	61	19	12	9	41	34	17	7
Ph_1Py_1	66	20	10	4	43	39	13	5
$Ph_1Py_{1.5}$	66	27	6	2	43	38	15	4

e. Elemental composition analysis

Table S6. Inductively coupled plasma-optical emission spectroscopy (ICP-OES) analysis—relative percentage amount of Mg in Ph_1Py_x.

Sample	Mg (wt. %)
Ph_1Py_0	0.154
$Ph_1Py_{0.5}$	0.125
Ph_1Py_1	0.144
$Ph_1Py_{1.5}$	0.106

Table S7. Energy-dispersive X-ray spectroscopy (EDS) elemental quantification of Ph_1Py_x.

Sample	Element (wt.%) ± standard deviation (wt.%)				
	N	C	O	Cl	Mg
Ph_1Py_0	6.3 ± 0.3	84 ± 0.3	7.77 ± 0.10	1.84 ± 0.06	0.17 ± 0.03
$Ph_1Py_{0.5}$	8.3 ± 0.3	85 ± 0.3	4.41 ± 0.09	2.41 ± 0.07	0.16 ± 0.03
Ph_1Py_1	5.4 ± 0.3	83 ± 0.3	9.20 ± 0.11	1.67 ± 0.05	0.14 ± 0.02
$Ph_1Py_{1.5}$	8.6 ± 0.3	82 ± 0.3	6.48 ± 0.10	2.47 ± 0.07	0.1 ± 0.3

Table S8. Organic elemental analysis of N, C, and H atoms and calculated C/N ratios.

Sample	Element (at. %)		C/N ratio (at. %)
	N	C	
Ph_1Py_0	7.01	54.6	7.79
$Ph_1Py_{0.5}$	6.45	52.4	8.12
Ph_1Py_1	8.19	63.0	7.69
$Ph_1Py_{1.5}$	7.95	59.6	7.49

f. Thermogravimetric analysis (TGA)

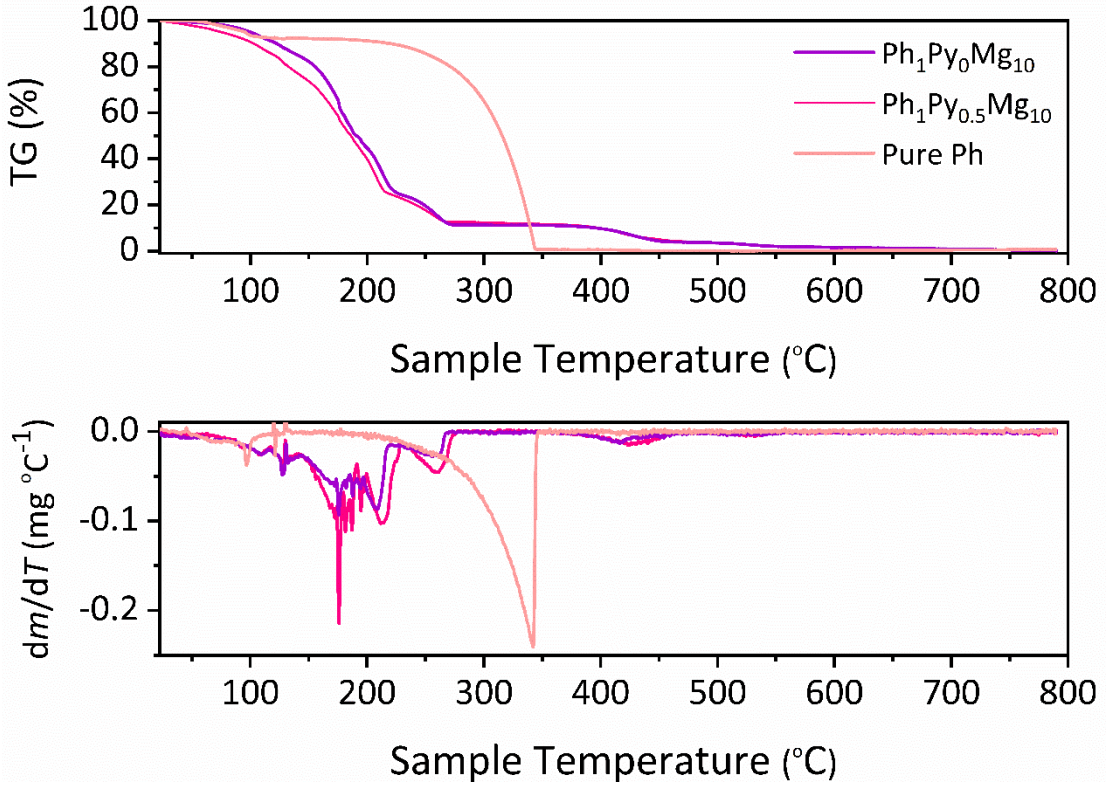

Fig. S6 TGA analysis of pure Ph and the starting materials (without washing of the templating agent). (a) TGA plot ($m\ m_0^{-1}$ (%) *vs* T), and (b) the calculated derivatives (dm/dT).

The observed weight losses are likely associated with the dehydration of magnesium chloride hexahydrate.[1,8] Notably, $Ph_1Py_{0.5}$ exhibits a more pronounced weight loss compared to Ph_1Py_0 during the measurement, likely related to partial evaporation of pyrene during the synthesis.[9] The lack of any additional weight loss attributable to the pyrene addition, along with the similar weight loss temperatures observed in both samples imply that pyrene does not introduce new decomposition steps but rather follows the same thermal pathway and is only partially removed during synthesis.

g. N_2 physisorption

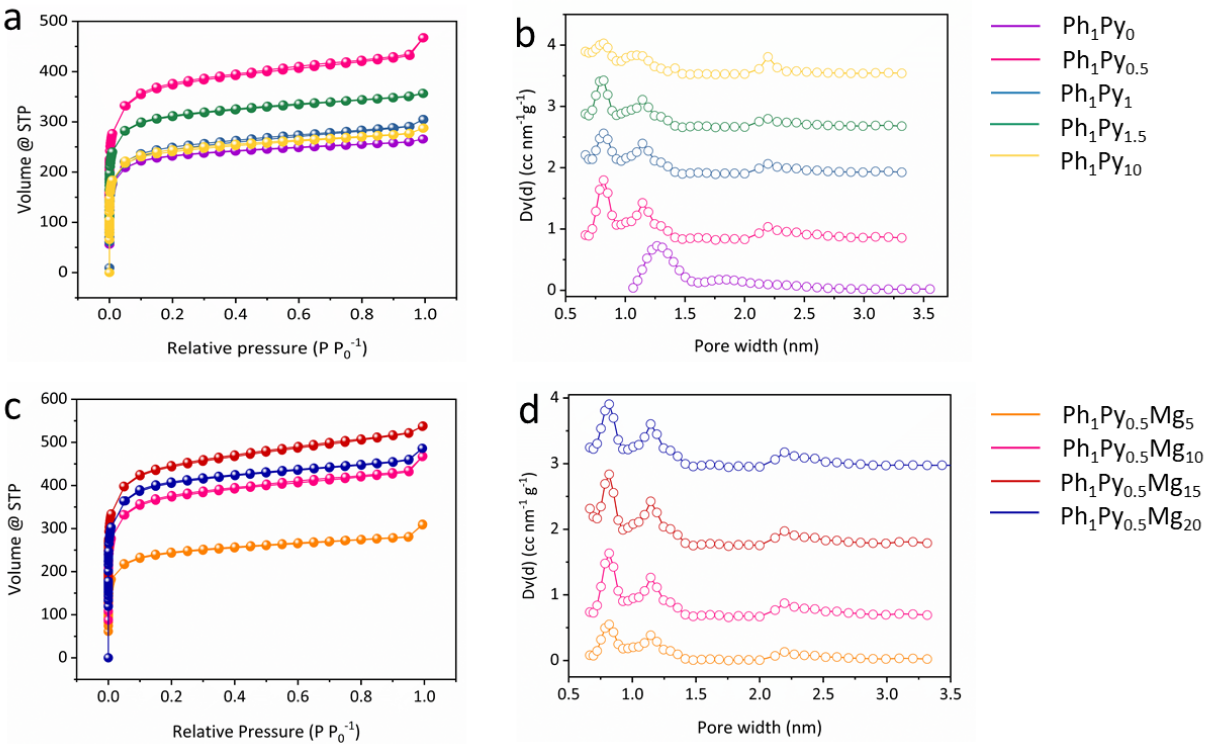

Fig. S7 N_2 physisorption measurements and analysis of (a–b) Ph_1Py_x and (c–d) $Ph_1Py_{0.5}Mg_t$. The adsorption isotherms (a, c) and pore size distribution (PSD) analysis (b, d) are shown. The specific surface area (SSA) values are calculated using the BET model and tabulated in Table S9.

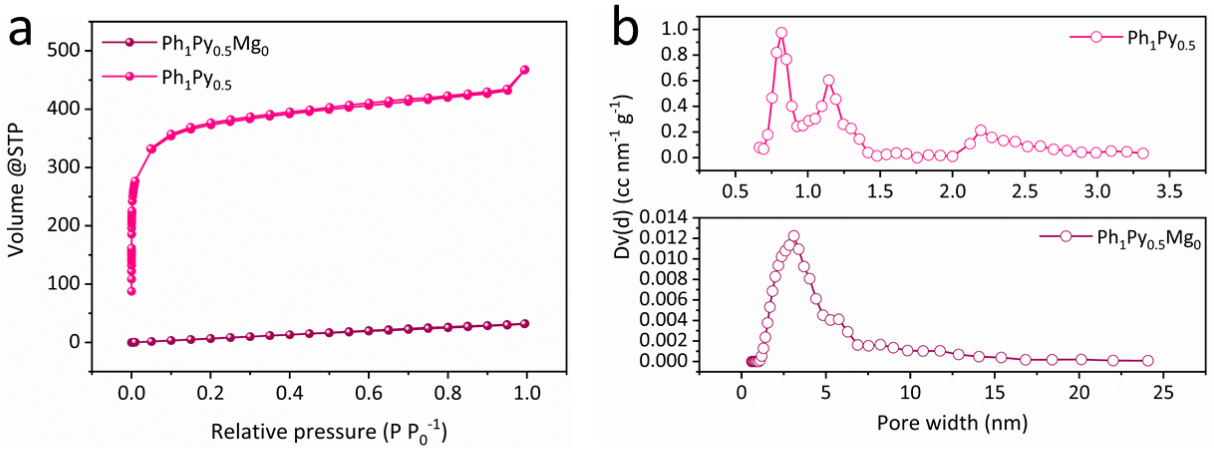

Fig. S8 N_2 physisorption measurements and analysis of $Ph_1Py_{0.5}$ and $Ph_1Py_{0.5}Mg_0$. The adsorption isotherms (a) and pore size distribution (PSD) analysis (b) are shown. The specific surface area (SSA) values are calculated using the BET model and tabulated in Table S9.

Table S9. N_2 physisorption analysis of Ph_1Py_x and $Ph_1Py_{0.5}Mg_t$. The specific surface area (SSA) was obtained from Brunauer–Emmett–Teller (BET) method. The relative contributions of micropores and mesopores were determined from the cumulative pore volume distribution across the full relative pressure range. Micropore volume was assigned to pores with ≤ 2 nm diameters,[10] while mesopore volume was estimated based on the cumulative volume of pores with diameter exceeding 50 nm above 2 nm diameter.

Sample	Mass ratio (m_{Mg} m_{Ph}^{-1})	SSA_{BET} (m^2 g^{-1})	Pore volume (cm^3 g^{-1})		Pore diameters (nm)
			$V_{micro,\ QSDFT}$	$V_{meso,\ QSDFT}$	
$Ph_1Py_{0.5}Mg_0$	0	0.63×10^2	—		3.09
$Ph_1Py_{0.5}Mg_5$	5	9.62×10^2	0.30	0.07	0.82, 1.14, 2.19
Ph_1Py_0	10	8.83×10^2	—		1.27, 1.85
$Ph_1Py_{0.5}$		1.40×10^3	0.45	0.17	0.82, 1.14, 2.19
Ph_1Py_1		1.15×10^3	0.39	0.12	0.82, 1.14, 2.19
$Ph_1Py_{1.5}$		1.19×10^3	0.39	0.11	0.82, 1.14, 2.19
Ph_1Py_{10}		9.21×10^2	0.29	0.07	0.82, 1.14, 2.19
$Ph_1Py_{0.5}$ (900 °C synthesis)		1.20×10^3	0.38	0.09	0.82, 1.14, 2.19
$Ph_1Py_{0.5}Mg_{15}$	15	1.62×10^3	0.55	0.12	0.82, 1.14, 2.19
$Ph_1Py_{0.5}Mg_{20}$	20	1.53×10^3	0.50	0.11	0.82, 1.14, 2.19

Both the adsorption isotherms and PDS showcase the exitance of micropores (< 2 nm) in the materials.[10] Addition of Py to the reactants (*i.e.*, $x \geq 0.5$ in Ph_1Py_x) results in the formation of new mesopore (> 2 nm) and new micropores.

As shown in Table S9, the SSA increases with Mg content up to a 15-fold excess, beyond which further Mg addition leads to a decline. PSD analysis reveals that higher Mg content results in increased micropore volume up to a 15-fold Mg excess while increasing the Mg content results in reduction in the mesopores volume.

h. Optical contact angle (OCA)

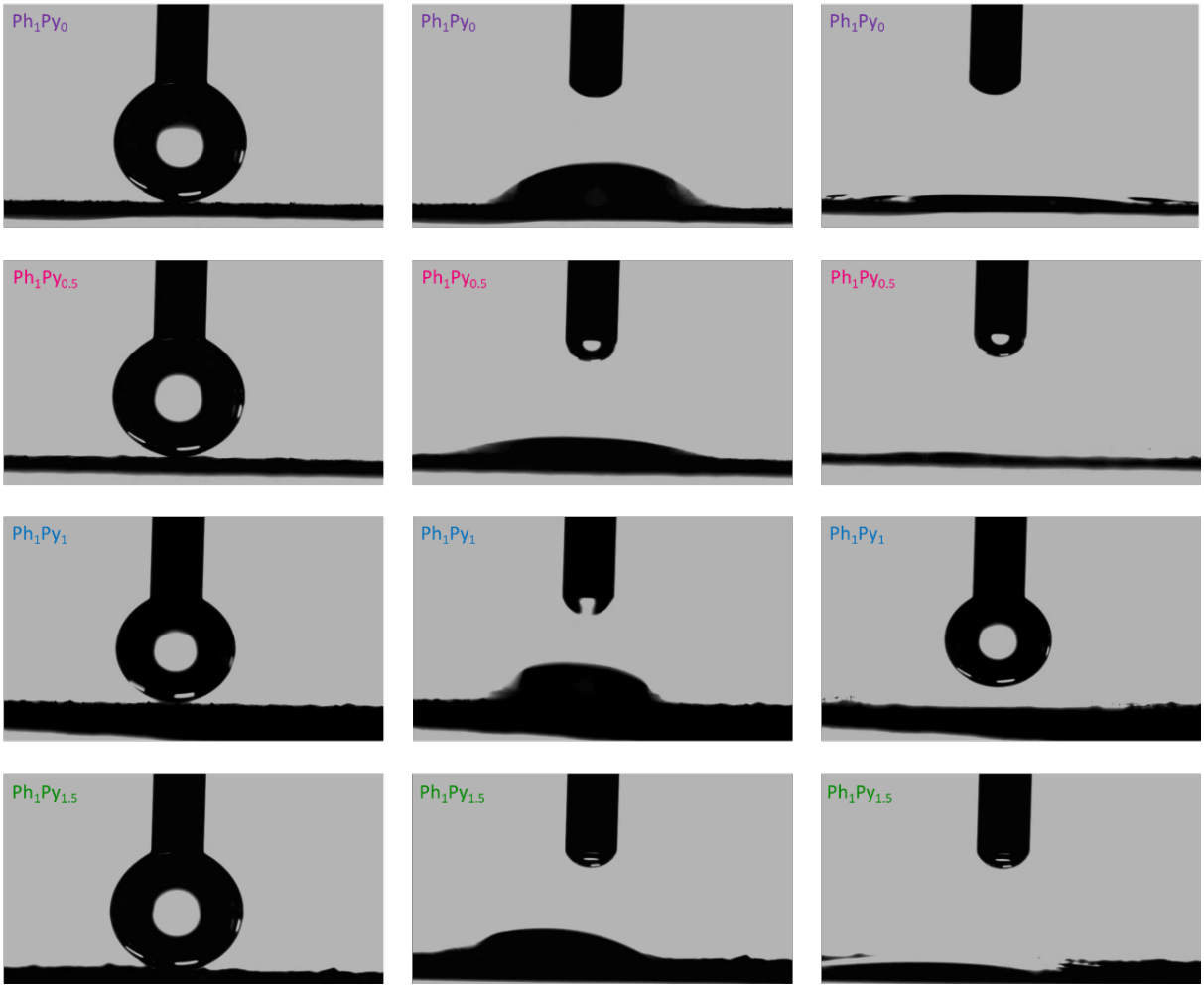

Fig. S9 OCA of Ph_1Py_x. The different stages (from left to right) during the measurements are shown for each of the four materials.

Table S10. OCA analysis of Ph_1Py_x and $Ph_1Py_{0.5}Mg_t$.

Sample	Mass ratio ($m_{Mg}\ m_{Ph}^{-1}$)	Mean contact angle	Standard deviation	CA
Ph_1Py_0	10	31.4°	7.20°	31° ± 7°
$Ph_1Py_{0.5}$		20.6°	4.24°	21° ± 4°
Ph_1Py_1		29.1°	4.93°	29° ± 5°
$Ph_1Py_{1.5}$		32.9°	6.90°	33° ± 7°
$Ph_1Py_{0.5}Mg_5$	5	30.5°	9.31°	31° ± 9°
$Ph_1Py_{0.5}Mg_{15}$	15	23.1°	9.60°	23° ± 10°
$Ph_1Py_{0.5}Mg_{20}$	20	22.2°	3.47°	22° ± 3°

i. Scanning electron microscopy (SEM)

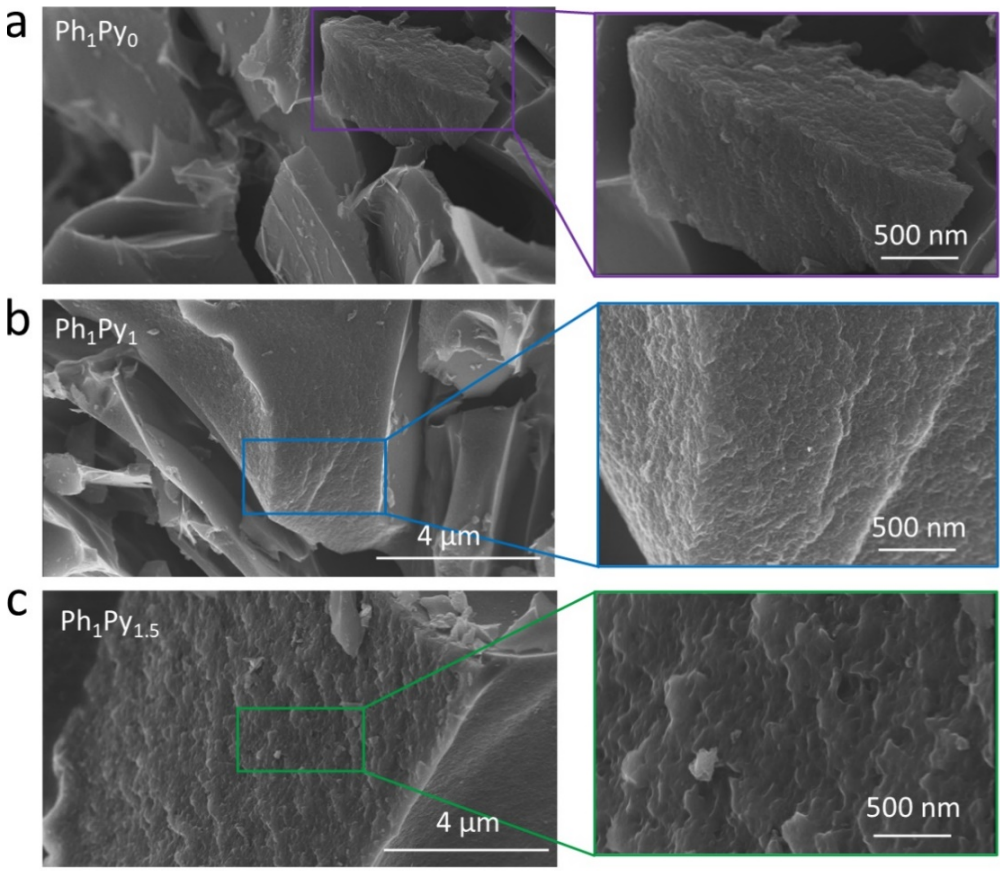

Fig. S10 SEM images at low and high magnifications: Ph_1Py_x, (a) Ph_1Py_0 (purple), (b) Ph_1Py_1 (blue), and (c) $Ph_1Py_{1.5}$ (green). $Ph_1Py_{0.5}$ (pink) electrodes

The SEM images in Fig.S9d–e illustrate the similarity in the observed morphologies before and after the electrochemical operation.

j. Scanning/ transmission electron microscopy (S/TEM)

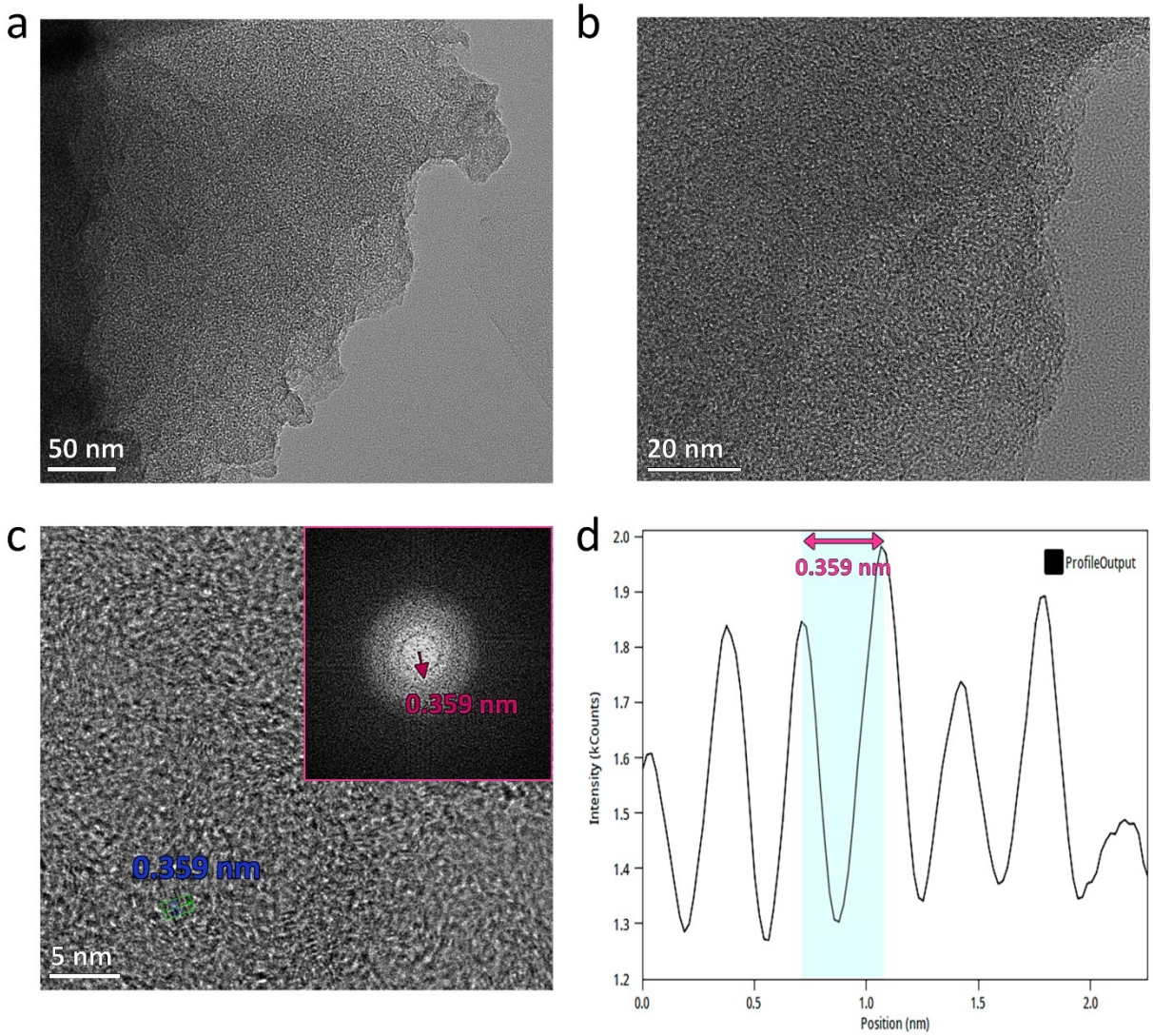

Fig. S11 $Ph_1Py_{0.5}$ TEM images: (a–b) at low magnifications, (c) high magnification; inset: FFT analysis of the image. (d) Intensity profile of the area marked in green in (c).

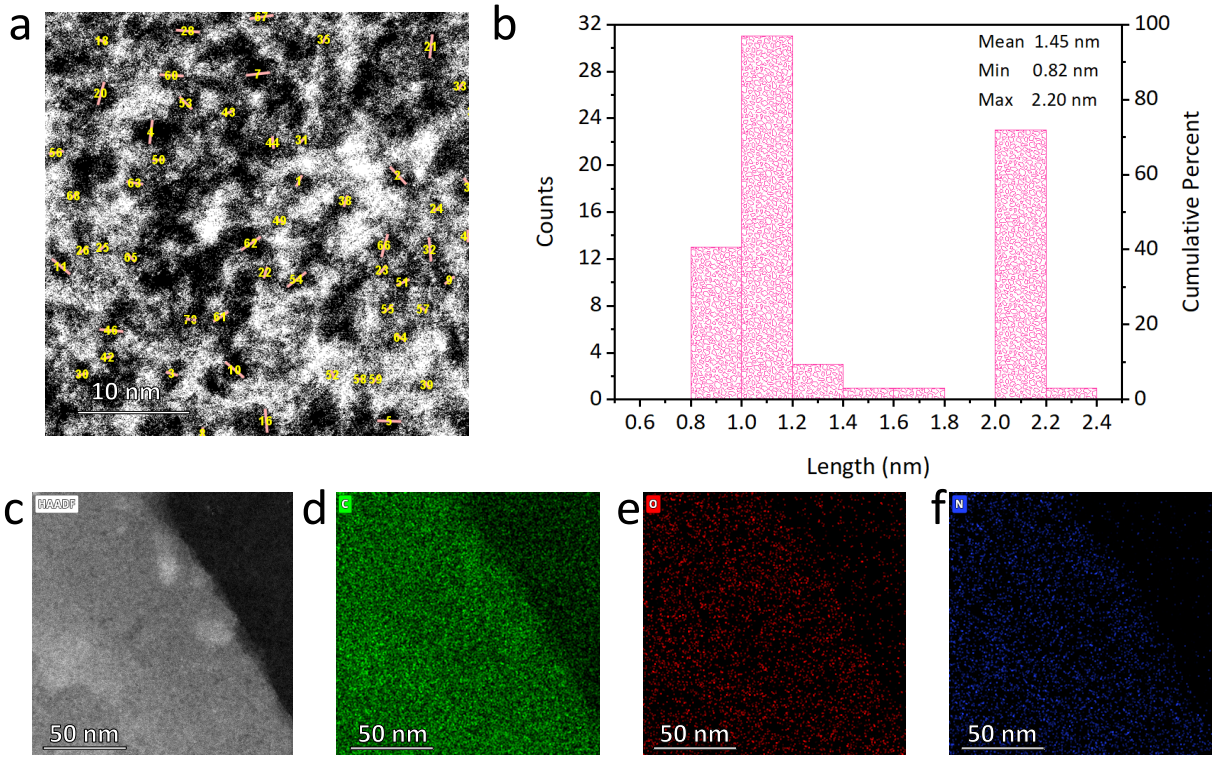

Fig. S12 $Ph_1Py_{0.5}$ HAADF STEM images. (a) Contrast-adjusted image (also shown in Fig. 1g), showing the 73 measured pore diameters (marked using yellow arrows) that were used for size distribution analysis. (b) Corresponding histogram of pore diameters extracted from Fig. S11b. (c–f) HAADF STEM image and the corresponding EDS elemental maps (N—blue, C—green, and O—red) of $Ph_1Py_{0.5}$.

6. Evaluation in a Three-Electrode Assembly

a. Specific capacitance (C_{sp}), specific energy (E_{sp}), and specific power (P_{sp})

The specific capacitance (C_{sp}) was calculated from cyclic voltammetry (CV) curves at different scan rates using Equation S5:[11,12]

$$C_{sp} = \frac{\int I dV}{2 \times m \times v \times \Delta V} \qquad \text{(Eq. S5)}$$

Where C_{sp} is the specific capacitance (F g^{-1}), $\int I dV$ is the integrated area under a CV curve, m is the mass of the active material (g), v is the scan rate (mV s^{-1}), and ΔV is the potential window (V).

The C_{sp} value is also calculated *via* GCD measurements using Equation S6:

$$C_{sp} = \frac{I \times \Delta t}{m \times \Delta V} \quad \text{(Eq. S6)}$$

Where C_{sp} is the specific capacitance (F g^{-1}), I is the applied constant current (A), Δt is the discharge time (s), m is the mass of the active material, and ΔV is the potential window (V).

The specific energy and specific power of $Ph_1Py_{0.5}$ and YP-50F activated carbon (AC) values are extracted from the GCD curve of each sample, using Equations S7 and S8, respectively:[11,12]

$$E_{sp} = C_{sp} \times \frac{\Delta V^2}{2 \times 3600} \qquad \text{(Eq. S7)}$$

$$P_{sp} = E_{sp} \times \frac{3600}{\Delta t^2} \qquad \text{(Eq. S8)}$$

Where E_{sp} is the specific energy (Wh kg^{-1}) , P_{sp} is the specific power (W kg^{-1}), C_{sp} is the specific capacitance (F g^{-1}), ΔV is the potential window (V), Δt is the discharge time (s), and 3600 is a unit conversion factor (h to s).

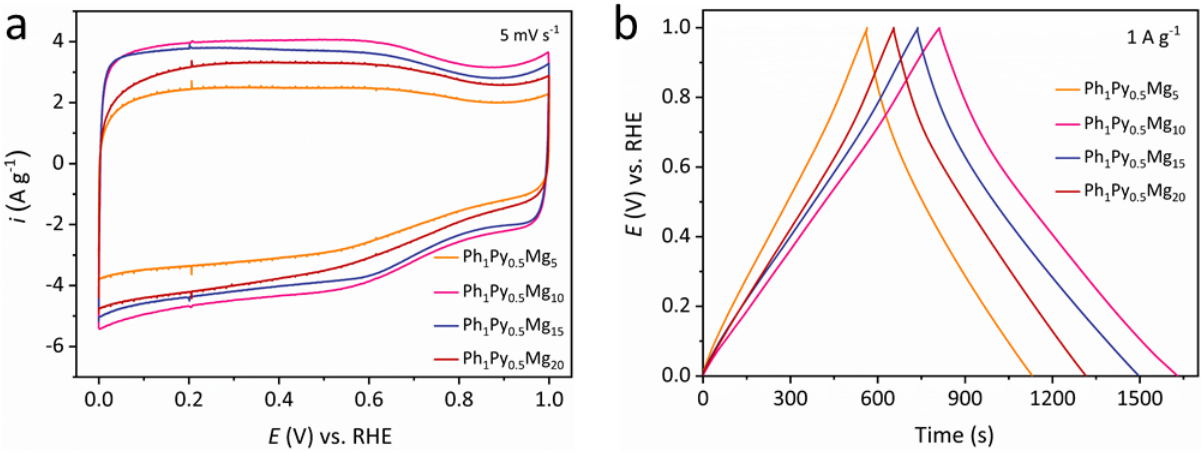

Fig. S13 Electrochemical performance of $Ph_1Py_{0.5}Mg_t$ electrodes. (a, b) Comparative cyclic voltammetry (CV) and galvanostatic charge–discharge (GCD) profiles for $Ph_1Py_{0.5}Mg_t$ electrodes at a scan rate of 5 mV s^{-1} and a current density of 1 A g^{-1}, respectively.

Table S11. Supercapacitive properties of different weight ratios of Ph_1Py_x and $Ph_1Py_{0.5}Mg_t$ electrodes, determined from cyclic voltammograms (CV) at 5 mV s^{-1} scan rate and galvanostatic charge–discharge (GCD) at 1 A g^{-1}. The parameters are extracted from Figures 2a, 2b, and S13.

Sample	Mass ratio (m_{Mg} m_{Ph}^{-1})	From CV C_{sp} (F g^{-1})	From GCD C_{sp} (F g^{-1})
Ph_1Py_0	10	506	610
$Ph_1Py_{0.5}$		748	818
Ph_1Py_1		496	586
$Ph_1Py_{1.5}$		561	645
$Ph_1Py_{0.5}Mg_5$	5	484.3	585
$Ph_1Py_{0.5}Mg_{15}$	15	694	752
$Ph_1Py_{0.5}Mg_{20}$	20	612	668

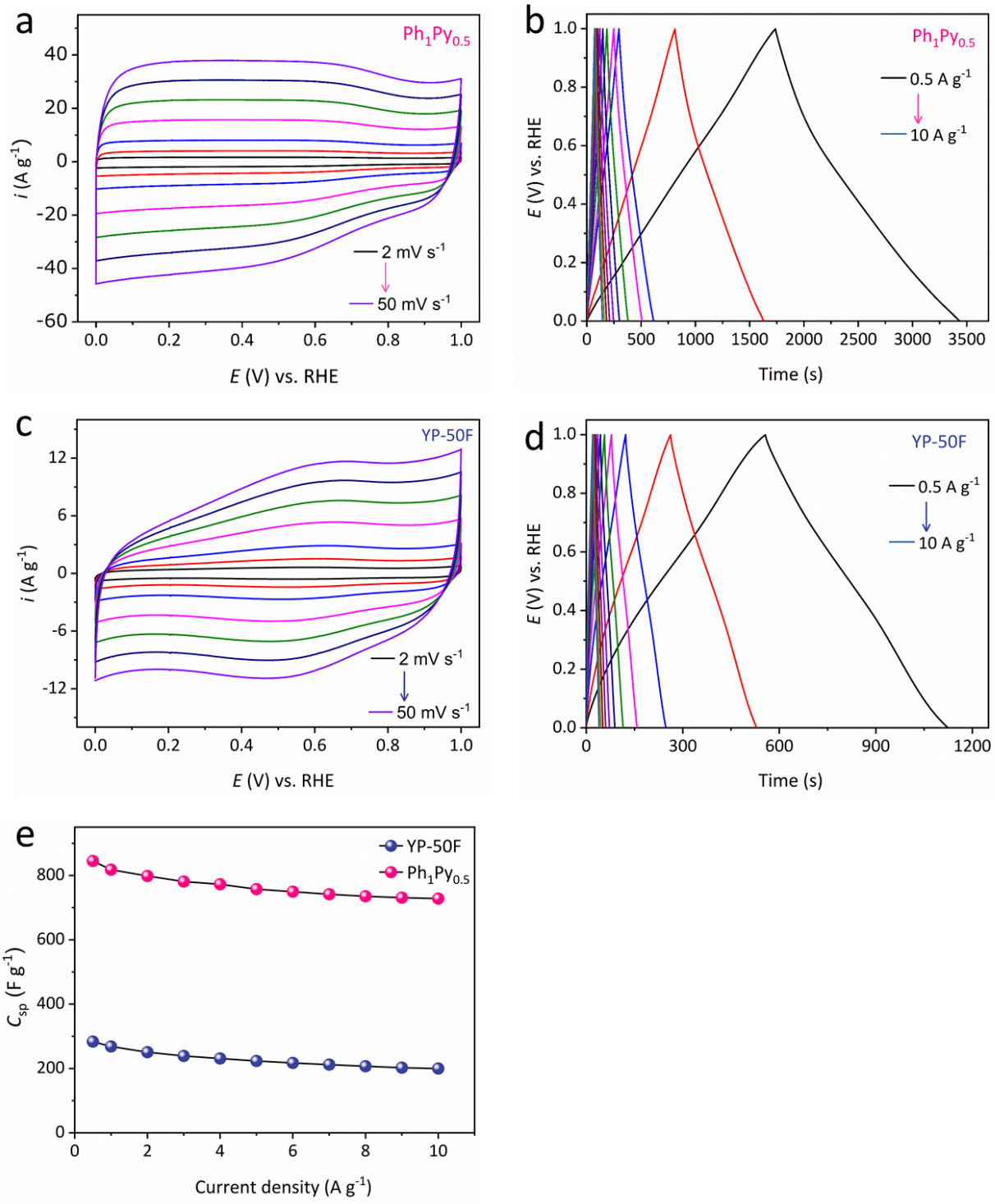

Fig. S14 Rate capability study showing the rate profiles for YP-50F and $Ph_1Py_{0.5}$ electrodes. (a, c) CV, (b, d) GCD, (e) Rate profiles derived from the CV measurements.

Table S12. Comparison of supercapacitive parameters—specific energy (E_{sp}) and specific power (P_{sp}) of $Ph_1Py_{0.5}$ and YP-50F AC, determined using the GCD method at 1 A g^{-1} (areal mass loading (*i.e.*, mass loading per electrode area) of ~0.42 mg cm^{-2}).

Electrode	From galvanostatic charge–discharge (GCD)		
	C_{sp} (F g^{-1})	E_{sp} (Wh kg^{-1})	P_{sp} (W kg^{-1})
$Ph_1Py_{0.5}$	818	113.6	500
YP-50F (AC)	268	37.28	500

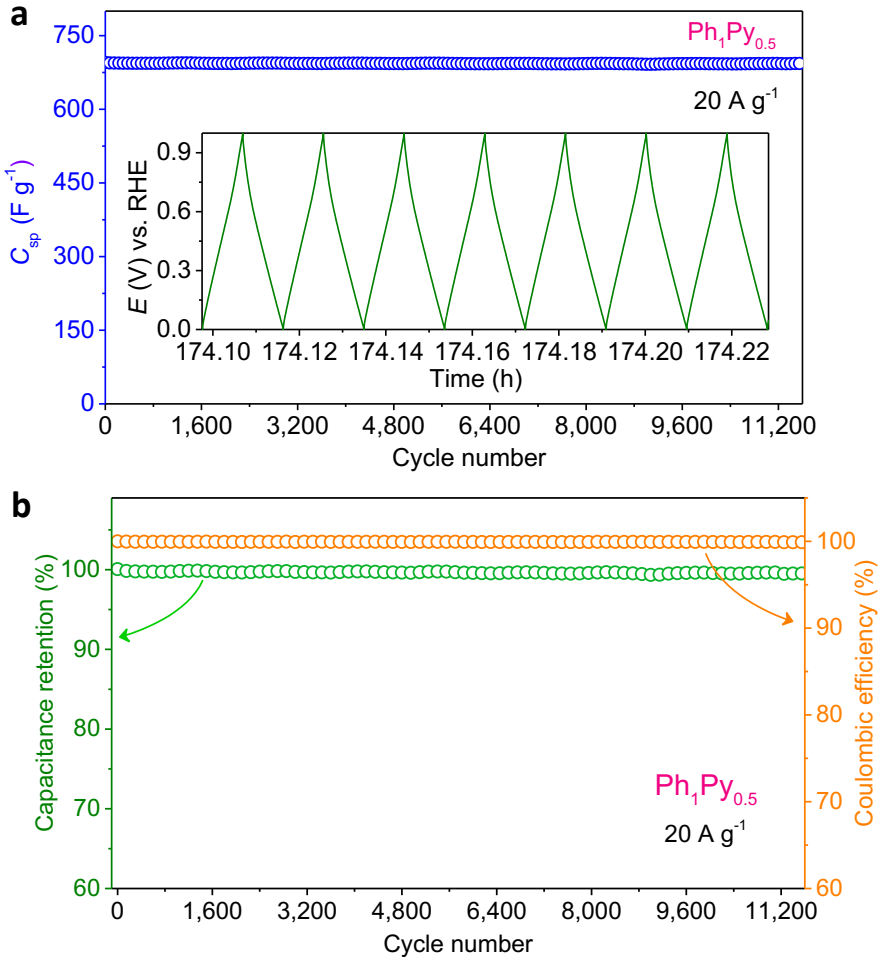

Fig. S15 Long-term cycling study. (a) Variation of specific capacitance with the number of cycles (> 1.1×10^4 cycles) at a rate of 20 A g^{-1} for the $Ph_1Py_{0.5}$ electrode. The inset shows a portion of the charge–discharge curves recorded on the 8th day of continuous cycling. (b) Capacity retention and Coulombic efficiency of the $Ph_1Py_{0.5}$ electrode over 11,500 cycles at a rate of 20 A g^{-1}. The supporting electrolyte is N_2-saturated 0.5 M H_2SO_4.

b. Capacitive contribution analysis

The Dunn method is used to extract the capacitive current and diffusion-controlled current (pseudo-SC). At a specific potential the current density can be expressed using Equation S9:[11–13]

$$i = k_1 v + k_2 v^{1/2} \quad \text{(Eq. S9)}$$

Where $k_1 v$ and $k_2 v^{1/2}$ correspond to the current contributions from the surface capacitive effects and the diffusion-controlled process, respectively.[11]

The *b*-value is used to determine if the current response is capacitive or diffusive. Equation S10 describes the relationship between current and scan rate:

$$i = a v^b \quad \text{(Eq. S10)}$$

Where *i* is the current at a specific voltage, v is the scan rate, and *a* and *b* are empirical constants. Applying a 10-base logarithm on both sides of Equation S8 allows to extract the slope *b* as shown in Equation S11:

$$\log(i) = \log(a) + b\log(v) \quad \text{(Eq. S11)}$$

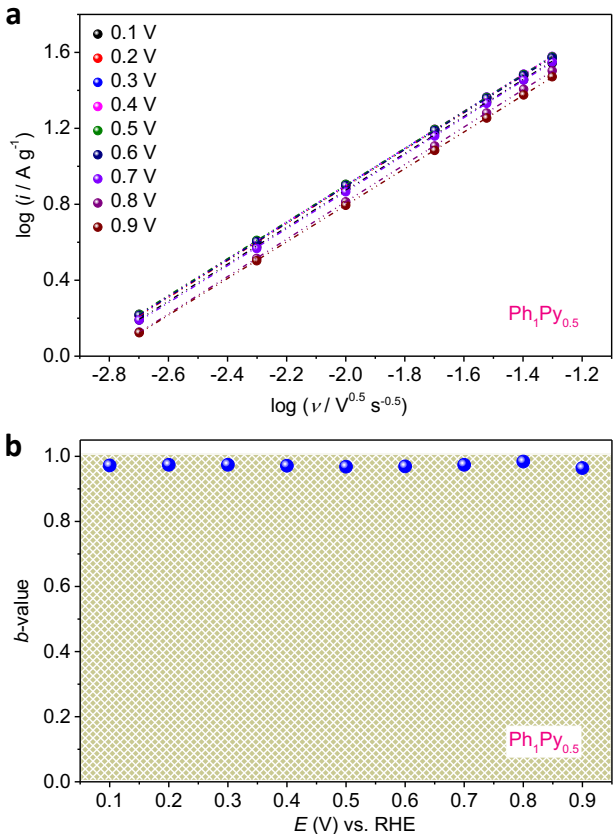

Fig.S16. Logarithmic relationship between currents and scan rates. (a) Logarithmic relationship between currents obtained from cyclic voltammograms and scan rates for $Ph_1Py_{0.5}$. (b) Calculated *b*-values for $Ph_1Py_{0.5}$ at different potentials. The *b*-values are extracted from Fig.S16a by determining the slope values.

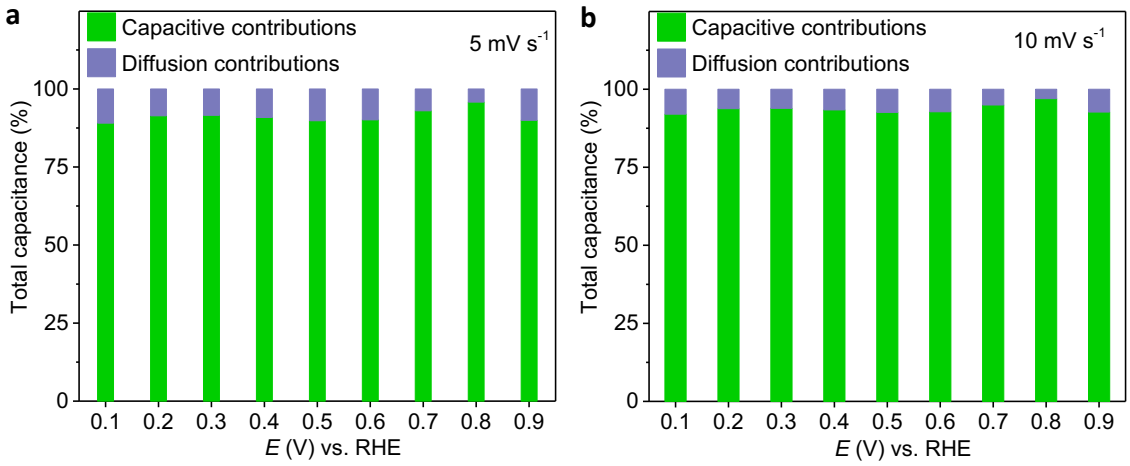

Fig. S17 A histogram plot showing the percentage of capacitive and diffusion contributions at a scan rate of (a) 5 mV s^{-1}, and (b) and 10 mV s^{-1} for $Ph_1Py_{0.5}$ at different potentials. Capacitive currents (blue-shaded regions) and diffusion-controlled currents (green-shaded regions) are derived from the total current.

c. Surface charge study

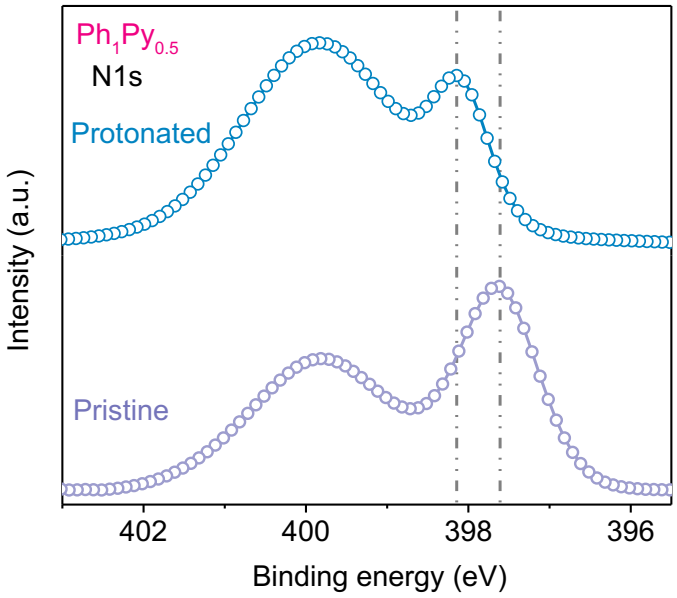

Fig. S18 N 1s XPS raw spectra for pristine $Ph_1Py_{0.5}$ and protonated $Ph_1Py_{0.5}$.

Table S13. Relative abundance (atomic percentage) of nitrogen species (from N 1s XPS analysis) in pristine and protonated $Ph_1Py_{0.5}$.

Sample	**Pristine $Ph_1Py_{0.5}$**				**Protonated $Ph_1Py_{0.5}$**			
Species	**N_1**	**N_2**	**N_3**	**N_4**	**N_1**	**N_2**	**N_3**	**N_4**
	Pyridine	Pyrrole	Graphite	N–O_x	Pyridine	Pyrrole	Graphite	N–O_x
Binding energy (eV)	398	399.5	400	401	398.5	400	401	402
Relative abundance (at. %)	48	21	24	6	29	35	29	7

The product $Ph_1Py_{0.5}$ (powder) was immersed in 0.5 M H_2SO_4 (the electrolyte used for SC measurements) for 96 h, followed by ambient drying for 24 h. The XPS surface N 1s spectra of both forms (pristine and protonated powders) was collected simultaneously under identical conditions. Since the N-containing form is Ph, the protonation of proton from the electrolyte can be represented as shown in Equation S12:

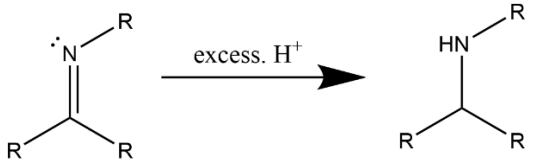

$R_1N{=}CR_2R_3 + H^+ \rightarrow R_1NH{-}C$ (Eq. S12)

d. Electrochemical impedance spectroscopy (EIS) calculations

An EIS study of $Ph_1Py_{0.5}$ and AC (YP-50F) is used to study the electrochemical behavior in the frequency domain. The imaginary capacitance (C'') component is obtained from the Nyquist plot *via* Equation S13:[11,12,14–17]

$$C''_{\text{img}} = -\frac{1}{2\pi \times f\,(\text{Hz}) \times Z''_{\text{img}}} \qquad \text{(Eq. S13)}$$

Where Z''_{img} is the imaginary part of the complex number Z, representing the capacitance, and f is the applied frequency.

A Bode plot is used to assess the power capability of the SC from the knee frequency (f_0) corresponding to the maximum of the imaginary part of the capacitance (C'') in the C'' *vs*

frequency plot. The inverse of the knee frequency is the relaxation time (τ_0), related to the minimal required time for the SC to fully discharge as shown in Equation S14:[11,12,14–17]

$$\tau_0 = \frac{1}{f_0} \qquad \text{(Eq. S14)}$$

Where τ_0 is the relaxation time (s) and f_0 is the knee frequency (Hz).

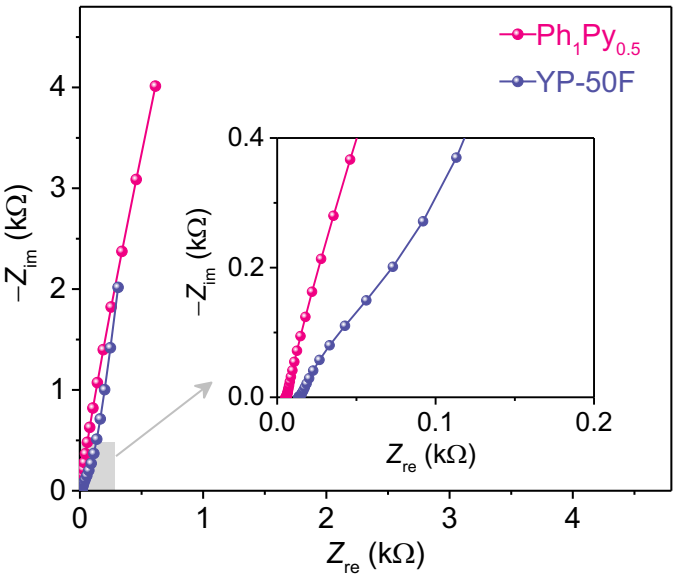

Fig. S19 Nyquist plots for YP-50F and $Ph_1Py_{0.5}$ electrodes at 0 V *vs* open-circuit voltage (OCV), acquired in the frequency range of 100 kHz to 5 mHz with a 10 mV (peak to peak) AC excitation signal. The inset shows the high frequency region of the EIS data.

Table S14. Knee frequency and relaxation time of YP-50F and $Ph_1Py_{0.5}$ electrodes determined using EIS. (The values are extracted from Fig.2i).

Electrodes	**''knee'' or ''onset'' frequency (f_0)**	
	f_0	τ_0
YP-50F	1.07 Hz	~935 ms
$Ph_1Py_{0.5}$	21.83 Hz	~45 ms

7. Device Fabrication and Testing (Asymmetric Cell)

Two-electrode cells were assembled using a $Ph_1Py_{0.5}$ electrode as the WE and a YP-50F activated carbon (AC) electrode as the CE, configured within a split test cell (MTI Corporation, USA). Three separators were immersed separately in 400 µL of 0.5 M H_2SO_4 for 30 minutes and added to the split cell. The stack was enclosed in a split test cell and assembled with a silicone O ring to prevent electrolyte evaporation and short circuiting. The two-electrode split test cell (Fig.3a) was then tested using a standard two-electrode measurement clip. After the measurements, the electrodes were washed with deionized water and air-dried. $Ph_1Py_{0.5}$ ink was prepared as follows: 50 mg of $Ph_1Py_{0.5}$, 5 mL IPA, and 0.15 mL of Nafion (5% wt.) solution was sonicated for 3 hours. For the AC ink, 200 mg of AC was mixed with 20 mL of IPA and 0.6 mL of 5% wt. Nafion solution, and the mixture was sonicated under identical conditions.

The ink was coated onto carbon paper sheets with a thickness of ~0.15 mm as supercapacitor electrodes (1.5 cm diameter), with mass loading of 4 mg cm^{-2} for $Ph_1Py_{0.5}$ electrode and 8 mg cm^{-2} for the AC electrode.

a. Specific capacitance (C_{sp}), capacity (Q_{sp}), energy (E_{sp}), and power (P_{sp})

The specific capacitance was calculated as was described earlier for the 3–electrode configurations using Equations S3–S4.

Q_{sp}, E_{sp}, and P_{sp} of $Ph_1Py_{0.5}$ and AC were calculated from the GCD profiles using Equations S15–S17, respectively:[11,12]

$$Q_{sp} = \frac{I \times \Delta t}{m_a} \qquad \text{(Eq. S15)}$$

Where I is the applied current (A), Δt is the discharge time (s), and m_a is the mass of the active material on one electrode (g). The specific capacity is measured in C g^{-1} units.

$$E_{sp} = \frac{I \times \Delta t \times \Delta V}{m_{total}} \qquad \text{(Eq. S16)}$$

Where I is the applied current (A), Δt is the discharge time (s), ΔV is the potential window (V), and m_{total} is sum of the mass of the anode and the mass of the cathode (g). The specific energy is measured in Wh g^{-1} units.

$$P_{sp} = \frac{I \times \Delta V}{m_{total}} \qquad \text{(Eq. S17)}$$

Where I is the applied current (A), ΔV is the potential window (V), and m_{total} is sum of the mass of the anode and the mass of the cathode (g). The specific power is measured in W g^{-1} units.

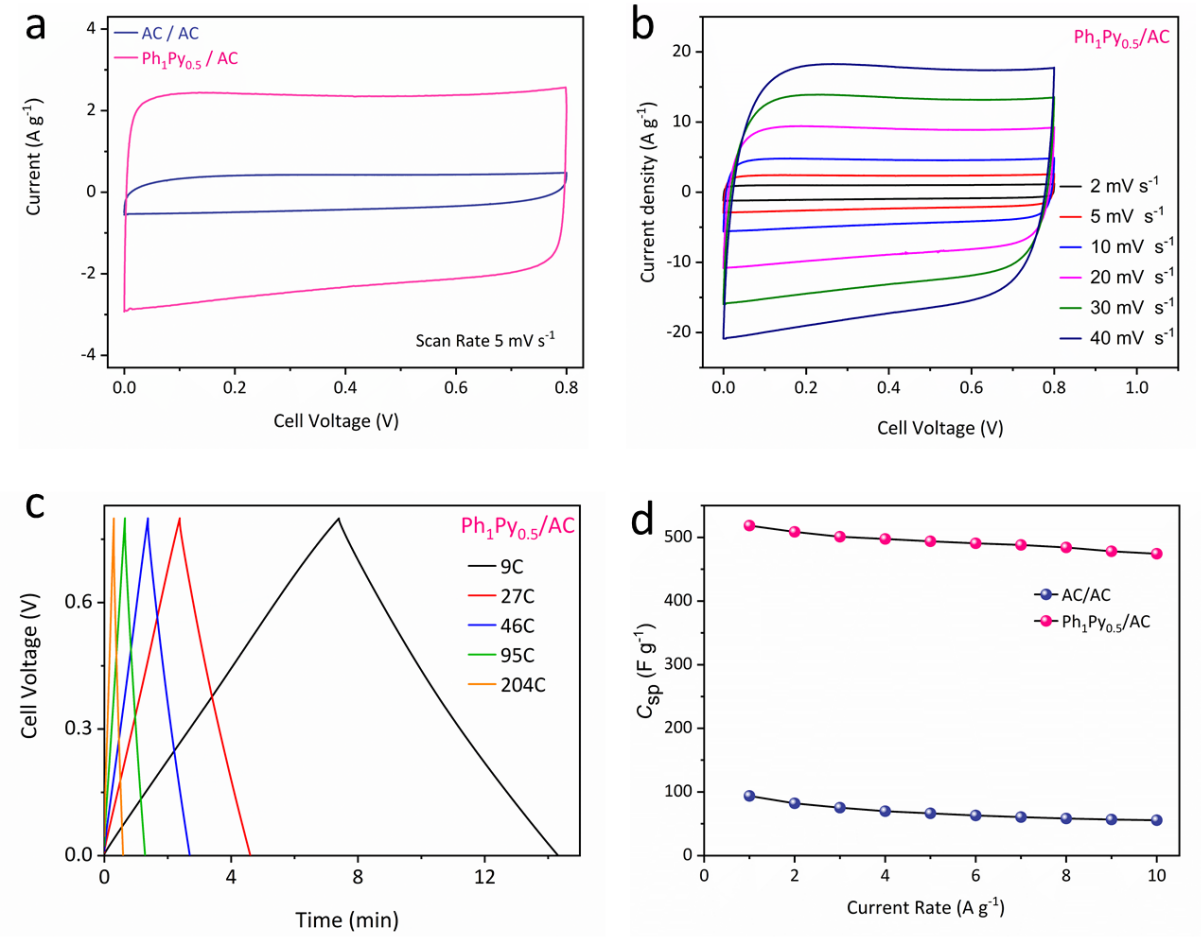

Fig. S20 Electrochemical performance in a two-electrode configuration, tested using a split test cell assembled with $Ph_1Py_{0.5}$ (+) electrodes and AC (–) electrodes. (a) Cyclic voltammetry profile of AC/AC and $Ph_1Py_{0.5}$/AC cells at a scan rate of 5 mV s^{-1}. (b) CV and (c) GCD profiles of the $Ph_1Py_{0.5}$/AC cell at different scan rates. (d) The corresponding specific capacity rate profile derived from the GCD profiles.

Table S15. Comparison of performance metrics of AC/AC and $Ph_1Py_{0.5}$/AC devices. The supercapacitive performance of AC/AC and $Ph_1Py_{0.5}$/AC devices is evaluated using galvanostatic charge–discharge (GCD) at 1 A g^{-1}. The data is obtained from Fig.2a.

Device	Specific Capacitance C_{sp} (F g^{-1})	Specific Capacity Q_{sp} (mAh g^{-1})	Specific Energy E_{sp} (Wh kg^{-1})	Specific power P_{sp} (W kg^{-1})
AC/AC	93.7	20.8	8.3	400
$Ph_1Py_{0.5}$/AC	518.5	115.2	30.7	267

Table S16. Performance comparison of the $Ph_1Py_{0.5}$ / AC cell device at different current rates.

Rate (A g^{-1})	Specific capacitance (F g^{-1})	Equivalent C-rate	Specific capacity (mAh g^{-1})	Specific energy (Wh kg^{-1})	Specific power (W kg^{-1})
1	518.5	9C	115.2	30.73	267
2	508.7	18C	113	30.14	533
3	499.9	27C	111.1	29.62	800
4	497.5	36C	110.6	29.48	1067
5	493.9	46C	109.7	29.27	1333
6	490.7	55C	109	29.08	1600
7	488.2	65C	108.5	28.93	1867
8	484.2	74C	107.6	28.69	2133
9	478.1	85C	106.3	28.33	2400
10	474.3	95C	105.4	28.10	2667
20	442.3	204C	98.29	26.21	5333
30	408.2	331C	90.71	24.19	8000
40	365.4	493C	81.2	21.65	10667
50	318.1	707C	70.69	18.85	13333

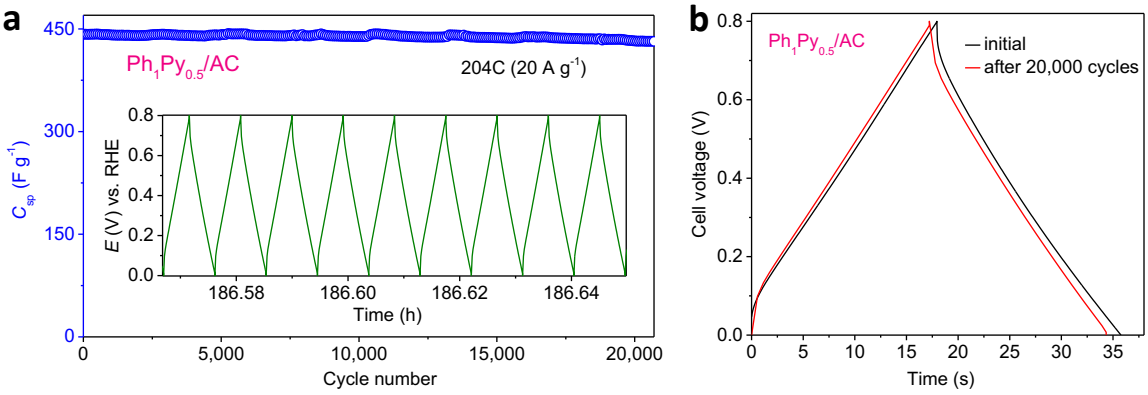

Fig. S21 Cycling test. (a) Variation of specific capacitance with the number of cycles at a rate of 20 A g^{-1} (204C) for the $Ph_1Py_{0.5}$/AC device over 20,000 cycles. The inset shows a portion of the charge-discharge curves recorded on the 8th day of continuous cycling. (b) Comparative galvanostatic charge-discharge profiles at the initial cycle and after 20,000 cycles.

8. Leakage and Self-Discharge Study (3-Electrode Configuration)

The self-discharge current (i_{sd}) is calculated using Equations S18–S20:[11,12]

$$C = C_{sp} \times m \qquad \text{(Eq. S18)}$$

$$i_{sd} = C \times \frac{V_1 - V_2}{\Delta t} \qquad \text{(Eq. S19)}$$

$$V_2 = \frac{V_1 + V_{OCV}}{2} \qquad \text{(Eq. S20)}$$

Where C is the capacitance, C_{sp} is the specific capacitance, m is the catalyst mass (10 μg) V_1 is the potential of the charged state, V_2 is the mean potential value and Δt is the time frame in which the potential drops to V_2. V_2 was calculated from the average open circuit potential (V_{OCV}) and V_1 (as defined in Equation S20).

Table S17. Leakage and self-discharge study in a 3-electrode configuration of $Ph_1Py_{0.5}$ and YP-50F (from Fig.2i).

Electrode materials	**YP-50F**	**$Ph_1Py_{0.5}$**
Open circuit voltage (V *vs* RHE)	0.58	0.73
Specific capacitance (F g^{-1})	268.4	818
Self-discharge current (μA)	36.79×10^{-3}	13.23×10^{-3}
Leakage current (mA F^{-1} V^{-1})	129.4×10^{-3}	67.08×10^{-3}

9. Post-Analysis Characterizations

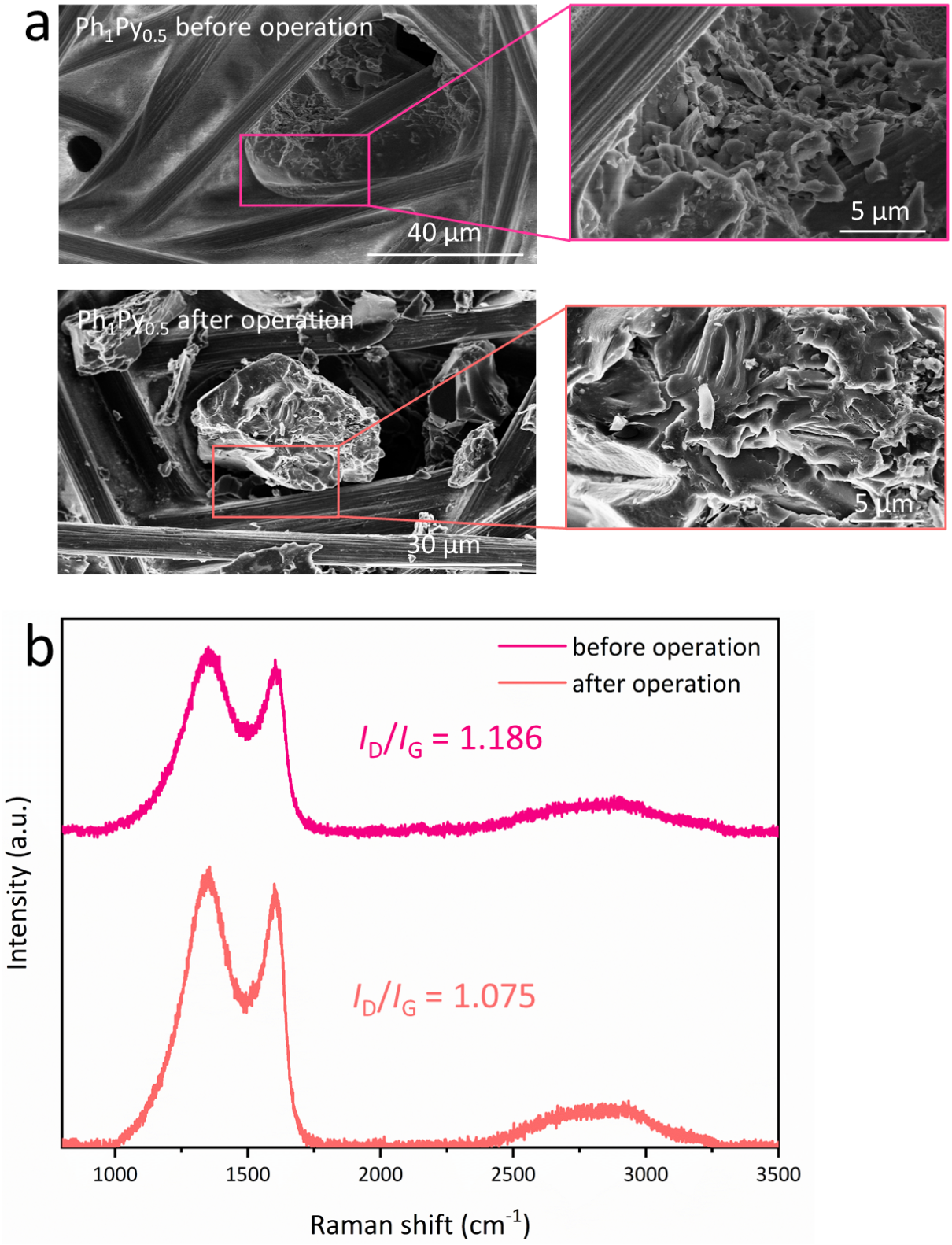

Fig. S22 $Ph_1Py_{0.5}$electrode before (pink) and after (orange) operation as SC: (a) SEM images at low and high magnifications. (b) Raman spectra of $Ph_1Py_{0.5}$ before and after operation as SC. The spectra are vertically offset for clarity.

10. Operational Assessment of the Device (Asymmetric Cell)

The electrochemical measurements were conducted in an H_2SO_4 aqueous electrolyte using two series-connected $Ph_1Py_{0.5}$/AC asymmetric configurations. The mass loadings were 4 mg cm^{-2} for $Ph_1Py_{0.5}$ and 8 mg cm^{-2} for AC. The electrode assembly followed the procedure described on page S30. Each electrode pair was individually charged via GCD up to 0.8 V. After charging, the pairs were connected in series and linked to the timer watch, as shown in the supplementary video.

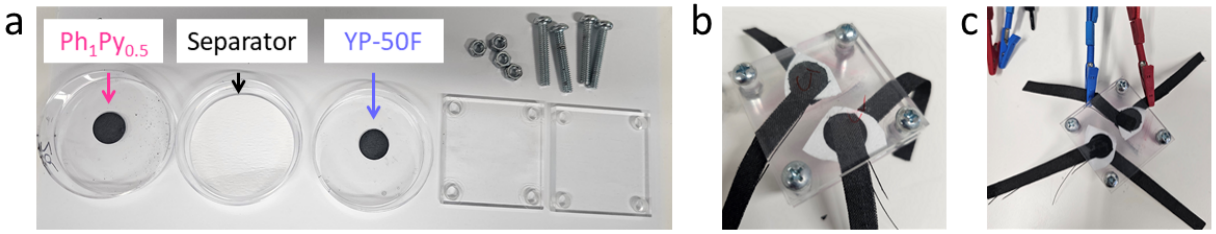

Fig.S23. Experimental validation of device functionality. (a–b) Images of the supercapacitor's structural components. (b) Fully assembled device. (c) Charging of the 2-electrode configuration to 0.8 V.

10. SC Properties Comparison

Table S18. Supercapcitive properties of active carbons and/or active materials synthesized using a templating method, reported in the literature.[2,10,18–34]

ESI Ref.	Main text Ref.	C_{sp} in 2-electrode configuration (F g^{-1}) / current rate (A g^{-1})	Active materials	Synthesis method
This work	This work	518.5 / 1	1,10-Phenanthroline and pyrene	Pyrolysis, hard and soft templating
10	7	136.3 / 1	Phenylenediamine	Template-free chemical activation
2	11	238 / 0.1	Melamine	Pyrolysis, hard and soft templating
18	64	41 / 0.2	Multi-heteroatoms co-doped porous carbon	Self-templating
19	69	112.8 / 1	Polyimide	Ultrasonic atomization-assisted ice templating
20	70	91.8 / 1	N, O, S-enriched carbon foam	Soft templating
21	71	66 / 1	PAC-KOH	Hard templating
22	72	234 / 0.5	Porous carbon spheres	Phenylenediamine-formaldehyde chemistry
23	73	118.9 / 0.5	Melamine	Microwave-assisted wet chemical synthesis
24	74	405 / 1	Polyethylene-Terephthalate urea	Thermal decomposition
25	75	81.7 / 1	Shrimp shell waste	Self–templating

26	76	44 / 0.5	ZIF-8@ZnO hybrids	Pyrolysis, activation with KOH
27	77	39 / 0.2	Quaternized lignin powder	Templating and activation
28	78	231.1 / 1	Polydopamine and silica nanoparticles	Hard templating
29	79	199 / 0.25	Resol-F127 micelles	Activation and foaming
30	82	231 / 0.1	*Euphorbia milii* plant waste	Hard templating
31	83	212 / 1	Liquefied wood	Soft-templating and chemical blowing
32	80	154 / 0.1	Chitosan, gelatine, and green algae	Template-free pyrolysis
33	81	85.1 / 0.1	Histidine and zinc gluconate	Hydrothermal reaction and pyrolysis
34	57	195.2 / 0.5	Bio-tar	Dual-activation of urea and KOH

11. Production Cost Estimation

The final production cost per gram was determined using the currency exchange rates as of October 29, 2025, provided by Google Finance (1 NIS = 0.3082 USD; 1 USD = 0.8589 EUR). The total production cost estimation (USD g^{-1}) accounts for the synthesis of $Ph_1Py_{0.5}$, the purchase of commercial activated carbon YP-50F (Table S18), and the energy consumption associated with the muffle furnace operation (Table S19). Based on the material production costs and the measured specific energy (E_{sp}) and specific power (P_{sp}) of the two-electrode device in both symmetric and asymmetric configurations (Table S14, ESI), the corresponding energy and power costs (Table S20 and Table S21, ESI) were subsequently calculated.

Initially, the production cost of $Ph_1Py_{0.5}$ was evaluated (Table S18). Prices of all precursors—matched by grade and purity—were obtained from the CAS SciFinder supplier database (https://scifinder.cas.org/, accessed October 2025). The final cost was expressed in USD g^{-1}, assuming that 1 L of 2 M HCl (prepared from a 32 wt.% HCl stock; density = 1.01 g mL^{-1}) was used in the synthesis. The cost of deionized (DI) water employed for washing was considered negligible in the calculation. The cost of YP-50F was taken as 1.78 USD g^{-1}, according to pricing for 100 g from the Kuraray website (Beyond Battery, https://beyond-battery.com/,accessed October 2025).

Subsequently, the electrical energy cost associated with the muffle furnace (model N 7/H, Nabertherm, Germany) was determined for the total duration of the synthesis across all stages (Table S19, ESI). The nominal heating power of the furnace (2.4 kW) was used to estimate energy consumption at each stage. The commercial electricity rate (0.0156 NIS kWh^{-1}) was obtained from the Israel Electric Corporation (IEC, https://www.iec.co.il/home, accessed October 2025). The final electrical cost was normalized to the mass of the synthesized $Ph_1Py_{0.5}$ (Table S18, ESI), under the assumption that six crucibles are processed simultaneously, thereby enhancing energy efficiency and reducing overall consumption.

Finally, the energy and power costs (USD Wh^{-1}) were calculated based on the total production costs of $Ph_1Py_{0.5}$ and YP-50F (Table S20 and Table S21, ESI), the mass of active materials used in assembling the two-electrode devices (both symmetric and asymmetric; see page S31, ESI), and the corresponding specific energy and specific power values provided in Table S14 of the ESI.

Table S19. Estimated cost per synthesis of $Ph_1Py_{0.5}$ and commercial YP-50F.

Material (purity/grade) CAS number	Supplier price[a]			Supply cost	Calculated cost per synthesis			
	Commercial quantity	Cost		(EUR g^{-1}) or (EUR mL^{-1})	*m* or *V*	(EUR g^{-1})	Product mass (g)	Total price (USD g^{-1})
		-	(EUR)					
1,10-Phenanthroline (>99%) 66-71-7	5 kg	937 USD	805.8	0.1612	4 g	0.6447	1.3101	**6.7**
Pyrene (95–98%) 129-00-0	25 kg	1450 USD	1247	0.0499	2 g	0.0998		
Magnesium chloride hexahydrate (>99%) 7791-18-6	25 kg	653 EUR	653	0.0261	40 g	1.0448		
HCl 32% wt. (AR grade) 7647-01-0	2.5 L	48. 5 EUR	48.5	0.0194	437 mL	8.4691		
AC (YP-50F)	100 g	178 USD	153	—			178	**1.78**
Total			2754	—	—	10.2583	—	—

[a]CAS SciFinder, Chemical Abstracts Service, American Chemical Society, https://scifinder.cas.org/, (accessed October 2025).

Table S20. Calculated cost of nitrogen oven operation during the synthesis.

Operation stage (assumed power rating)	**Manufacturing electrical power consumption (kW)**	**Calculated cost of operation**				
maximal (100%)	2.4	**Operation time (h)**	**Energy (kWh)**	**Price per kWh (USD)**	**Total duration cost (USD)**	**Total (USD g^{-1})**
ramping 2.5 °C min^{-1} (75%)	1.8	6.2	11.2	0.0048	0.0609	**0.00781**
Holding temperature (10%)	0.2	6.0	1.4			
Total	2.0	12.2	12.6			

Table S21. Energy and power supply required for the assembly of symmetric and asymmetric 2-electrode devices. The given total loading mass is the same as used for the synthesis (Page S30, ESI). The specific energy and specific power values are extracted from Table S15, ESI.

Device	**Total loading mass**		**Energy**			**Power**		
	(mg)	**(kg)**	**Specific Energy E_{sp} (Wh kg^{-1})**	**Energy E (Wh)**	**Energy E (kWh)**	**Specific power P_{sp} (W kg^{-1})**	**Power P (W)**	**Power P (kW)**
AC/AC	400	0.0004	8.3	0.00332	3.32	400	0.16	160
$Ph_1Py_{0.5}$/AC	250	0.00025	30.7	0.007675	7.675	267	0.06675	66.75

Table S22. Total energy cost and power cost of the symmetric and non-symmetric 2-electrode devices.

Calculated cost per synthesis		**Total energy cost (USD g^{-1})**		**Total power cost (USD W^{-1})**	
Material	**(USD g^{-1})**	**Energy E (Wh)**	**(USD Wh^{-1})**	**Power P (W)**	**(USD W^{-1})**
$Ph_1Py_{0.5}$	6.73	6.73	**90.0**	0.16	**10.4**
AC (YP-50F)	1.78	1.78	**214**	0.06675	**4.45**

Supplementary Information References

1 J. Xu, T. Li, T. Yan, J. Chao and R. Wang, *Sol. Energy Mater. Sol. Cells*, 2020, **219**, 110819.

2 J. Pampel, A. Mehmood, M. Antonietti and T. P. Fellinger, *Mater. Horiz*., 2017, **4**, 493–501.

3 W. Gan, P. Xiao and J. Zhu, *Catalysts*, 2023, **13**, 1132.

4 Y. Zhang, G. Ji, C. Li, X. Wang, A. Li, *Chem. Eng. J.*, 2020, **390**, 124398.

5 K.F. Kevin, M.H. John, *Phys. Chem. Chem. Phys.*, 2020, **22**, 24870-24886

6 Suzuki, Y., Hino, H., Hawai, T. *et al.*, *Sci Rep*, 2020, **10**, 21790.

7 F. Zheng, Y. Yang and Q. Chen, *Nat. Commun.*, 2014, **5**, 5261.

8 J. Barrio, A. Pedersen, S. C. Sarma, A. Bagger, M. Gong, S. Favero, C. X. Zhao, R. Garcia-Serres, A. Y. Li, Q. Zhang, F. Jaouen, F. Maillard, A. Kucernak, I. E. L. Stephens and M. M. Titirici, *Adv. Mater.*, 2022, **35**, 2211022.

9 J. Tzadikov, M. Amsellem, H. Amlani, J. Barrio, A. Azoulay, M. Volokh, S. Kozuch and M. Shalom, *Angew. Chem. Int. Ed.*, 2019, **58**, 14964–14968.

10 X. R. Zhang, T. B. Song, T. Le He, Q. L. Ma, Z. F. Wu, Y. G. Wang and H. M. Xiong, *Adv. Funct. Mater.*, 2024, **35**, 2419219.

11 S. Mukhopadhyay, A. R. Kottaichamy, M. C. Devendrachari, R. M. Mendhe, H. M. Nimbegondi Kotresh, C. P. Vinod and M. Ottakam Thotiyl, *Chem. Sci.*, 2023, **15**, 1726–1735.

12 A. R. Kottaichamy, S. Deebansok, J. Deng, M. A. Nazrulla, Y. Zhu, Z. M. Bhat, M. C. Devendrachari, C. P. Vinod, H. M. N. Kotresh, O. Fontaine and M. O. Thotiyl, *Chem. Sci*., 2023, **14**, 6383–6392.

13 J. Wang, J. Polleux, J. Lim and B. Dunn, *J. Phys. Chem. C*, 2007, **111**, 14925–14931.

14 K. Yang, K. Cho and S. Kim, *Sci. Rep*., 2018, **8**, 11989.

15 P. L. Taberna, P. Simon and J. F. Fauvarque, *J. Electrochem. Soc.*, 2003, **150**, A292.

16 Y. Yoo, M. S. Kim, J. K. Kim, Y. S. Kim and W. Kim, *J. Mater. Chem. A*, 2016, **4**, 5062–5068.

17 M. G. C. Munhoz, A. C. Rodrigues-Siqueli, B. C. S. Fonseca, J. S. Marcuzzo, J. T. Matsushima, G. F. B. Lenz e Silva, M. R. Baldan and G. Amaral-Labat, *Mater. Res.*, 2022, **25**, e20220142.

18 Q. D. Nguyen, Y. H. Wu, T. Y. Wu, M. J. Deng, C. H. Yang and J. K. Chang, *Electrochim. Acta*., 2016, **222**, 1153–1159.

19 B. Liang, L. Chen, J. Lv, Y. Li, W. Tan, W. Zhu, J. Hu, K. Zeng and G. Yang, *ACS Appl. Energy Mater*., 2022, **5**, 6163–6173.

20 H. Peng, B. Yao, X. Wei, T. Liu, T. Kou, P. Xiao, Y. Zhang and Y. Li, *Adv. Energy Mater.*, 2019, **9**, 1803665.

21 J. Xiao, H. Zhang, Y. Wang, C. Zhang, S. He and S. Jiang, *Front. Chem. Sci. Eng.*, 2023, **17**, 387–394.

22 M. Xu, Y. Liu, Q. Yu, S. Feng, L. Zhou and L. Mai, *Chin. Chem. Lett.*, 2021, **32**, 184–189.

23 B. Yan, H. Huang, X. Qin, S. Xiu, J. Choi, D. Ko, T. Chen, W. Zhang, B. Quan, G. Diao, X. Jin and Y. Piao, *ACS Appl. Energy Mater.*, 2021, **4**, 13735–13747.

24 N. A. Elessawy, J. El Nady, W. Wazeer and A. B. Kashyout, *Sci. Rep*., 2019, **9**, 1129.

25 O. P. Nanda, N. K. Das, P. Sekar, A. Ramadoss and B. Saravanakumar, *Bioresour. Technol. Rep*., 2022, **19**, 101198.

26 J. Huang, F. Hao, X. Zhang and J. Chen, *J. Electroanal. Chem.*, 2018, **810**, 86–94.

27 P. Feng, H. Wang, P. Huang, L. Zhong, S. Gan, W. Wang and L. Niu, *Chem. Eng. J.*, 2023, **471**, 144817.

28 Q. Zhang, C. Deng, Z. Huang, Q. Zhang, X. Chai, D. Yi, Y. Fang, M. Wu, X. Wang, Y. Tang and Y. Wang, *Small*, 2022, **19**, 2205725.
29 Q. Miao, Y. Xu, R. Kang and H. Peng, *J. Energy Storage*, 2022, **55**, 105590.
30 O. P. Nanda and S. Badhulika, *J. Energy Storage*, 2022, **56**, 106042.
31 Z. Wu, K. Zhang, C. Ma, S. Luo, W. Li and S. Liu, *J. Energy Storage*, 2023, **68**, 107619.
32 A. Ilnicka, M. Skorupska, M. Szkoda, Z. Zarach, P. Kamedulski, W. Zielinski and J. P. Lukaszewicz, *Sci. Rep.*, 2021, **11**, 18387.
33 G. Chen, Z. Liu, G. Yang, Q. Zhang, T. Lan, C. Zhang, P. Li, K. Liu and S. He, *Colloids Surf. A Physicochem. Eng. Asp.,* 2024, **687**, 133498.
34 J. Jia, Y. Sun, Z. Liu, Z. Liu, L. Huo, K. Kang, Y. Zhao, L. Zhao, T. Xie, M. Cao and Z. Yao, *Biochar*, 2023, **5**, 91.